



Research Project (PRe)

Major: Mechanics

Year: 2019

Detonation Initiation by Shock Wave Refraction

Author:

Yann de Gouvello

Class of:

2020

ENSTA Paris

supervisor:

Sabine Ortiz

Host organization

supervisor:

Rémy Mével

Internship dates: June 1 to August 23, 2019

Name of the host institution:

Tsinghua University Center for Combustion Energy

Address:

30 Shuang Qing road, 100084 Beijing, China

Résumé

L'objectif de ce projet était d'étudier un phénomène de combustion pouvant endommager un moteur à essence. Ceci a conduit à étudier la théorie de la réfraction d'onde de choc. Le projet s'est focalisé sur la théorie de réfraction d'une onde plane à un interface plan incliné, allant d'une phase gazeuse rapide à une phase gazeuse lente.

Une méthode pour prédire l'apparition de différents systèmes de chocs et d'expansions. Des résultats théoriques en appliquant cette méthode ont ensuite été confrontés à des simulations CFD d'un collaborateur. Dans la perspective de modéliser des cas avec des gaz réactifs, des particules lagrangiennes ont été étudiées.

Mots clés: combustion, automobile, mécanique des fluides, cliquetis, réfraction d'une onde de choc

Abstract

This internship's aim was to investigate the super-knock combustion mechanism, that can damage internal combustion engines. This lead to studying shock wave refraction, and more specifically slow-fast shock wave refraction at a plane interface. Previous papers were revisited to determine under which conditions refraction patterns may form. Theoretical results were confronted to a collaborator's CFD simulations. In the perspective of developing a theory with reactive phases, Lagrangian particles were considered.

Keywords: combustion, automotive engineering, fluid mechanics, knock, super-knock, shock wave refraction

Thank you to my parents, for supporting my education and welcoming me at their home

Thank you to Pr. Rémy Mével for guiding me during this internship at Tsinghua

Thank you to Pr. Sabine Ortiz for accepting to supervise my internship at ENSTA Paris

Thank you to Stany Gallier from ArianeGroup for providing finite element results

Thank you Vincent Ren, for giving me good company at work and helping me around China

Thank you to Yizhou and Yakun my lab colleagues

Thank you Fayo

Thank you Anouk

Contents

1	Introduction	8
2	Shock wave refraction at a plane interface	12
2.1	The plane shock wave refraction fundamentals	12
2.2	Plane shock theory applied to the incident shock wave	15
3	Refraction wave patterns and theoretical models	16
3.1	Frame of reference and i polar	16
3.2	Regular refraction	16
3.2.1	t polar	17
3.2.2	Membrane equilibrium	18
3.3	Regular refraction with a reflected expansion (RRE)	18
3.3.1	Transition from reflected expansion to reflected shock	19
3.4	Regular refraction with a reflected shock (RRR)	20
3.4.1	Transition from regular refraction to irregular refraction	21
3.5	Irregular refraction patterns	22
3.5.1	Piston theory to estimate precursor t-wave speed	22
3.5.2	Bound Precursor Refraction (BPR)	22
3.5.3	Transition from bound precursor to free precursor refraction	24
3.5.4	Free precursor patterns	25
3.5.5	Computing the k wave polar	27
3.5.6	Mach stem refraction	29
3.5.7	Lambda shock refraction	29
4	Refraction regime diagram in ω_i - χ plane	30
4.1	Refraction regime diagram for a CO_2-CH_4 slow-fast interface	30
4.2	Refraction regime diagram for a $Ar-He$ slow-fast interface	32
5	Shock wave refraction at an inert-reactive interface	35
5.1	Refraction regime diagram at a $2H_2+1O_2-He$ interface	35
5.2	Lagrangian particles in RRE flows	37
5.2.1	Initial conditions	37
5.2.2	Flow pattern	37
5.2.3	Before the expansion fan	37
5.2.4	In the expansion fan	37
5.2.5	Results	39
5.3	Predicting mixture ignition	40
5.3.1	Insufficiency of chemical thermodynamics	40
5.3.2	Kinetic criterion	40
6	Conclusion	42

7 Appendices**45**

Nomenclature

Gas parameters

I/II	Gas phases
m	Gas interface
$\mathcal{M}_{I/II}$	Molar masses
$T_{0,I/II}$	Temperatures of the gases at rest
P_0	Pressure of the gases at rest
$\gamma_{I/II}$	Isentropic coefficient
R_u	Universal gas constant
$R_{I/II}$	Gas constants

Shock wave indexes

i	Incident shock wave
r	Reflected wave
t	Transmitted shock wave
j	j precursor shock wave
k	k precursor shock wave
M	Mach stem

Initial shock wave conditions for refraction

ω	Angle of incidence
Ip	Endpoint of i shock
(LIp)	Ip trajectory line
χ	Shock strength
ω_i	Angle between i shock and (LIp)

General wave parameters

$\xi_{i/r/...}$	Shock pressure jump >1
$M_i/...$	Pre-shock Mach in Ip's frame of reference
$M_{si}/...$	Shock mach
$W_i/...$	Normal shock wave speed
P_1	Pressure behind incident shock
δ_1	Deviation behind incident i shock
P_2	Pressure behind reflected wave
δ_2	Deviation behind reflected r wave
P_t	Pressure behind transmitted t shock
δ_t	Deviation behind t wave

Lagrangian particle parameters

dV_m	Lagrangian particle
r_e, r_i	Distance to Ip
(x, y)	Initial particle positions
μ	Angle between expansion and particle speed vector
θ	Angle detailed in figure 5.3(a)
$u_{n/t}$	Particle speed normal/ tangential to expansion
P	Particle pressure
T	Particle temperature
V_m	Particle specific volume

Chemical parameters

K^o	Reaction equilibrium constant
$\Delta_r H^o$	Standard enthalpy of reaction
v	Reaction speed
k	Rate constant
c_i	Species concentration
E_a	Activation energy

Chapter 1

Introduction

Host institution presentation This internship was performed at Tsinghua University in Beijing, China and more specifically at the Center for Combustion Energy shown in fig 1.1. The Center of Combustion Energy (CCE) include 15 faculty and staff members, and is currently directed by Pr. Chung K. Law. Pr. Chung K. Law is an experienced combustion researcher, academician of the American Academy of Engineering.

Amongst the 15 faculty and staff members is my supervisor, Pr. Rémy Mével. He is a specialist in the domain of combustion chemical kinetics, working as an associate professor at the CCE. During this internship, I worked for him on the fluid mechanics of combustion, applied to automotive engineering.



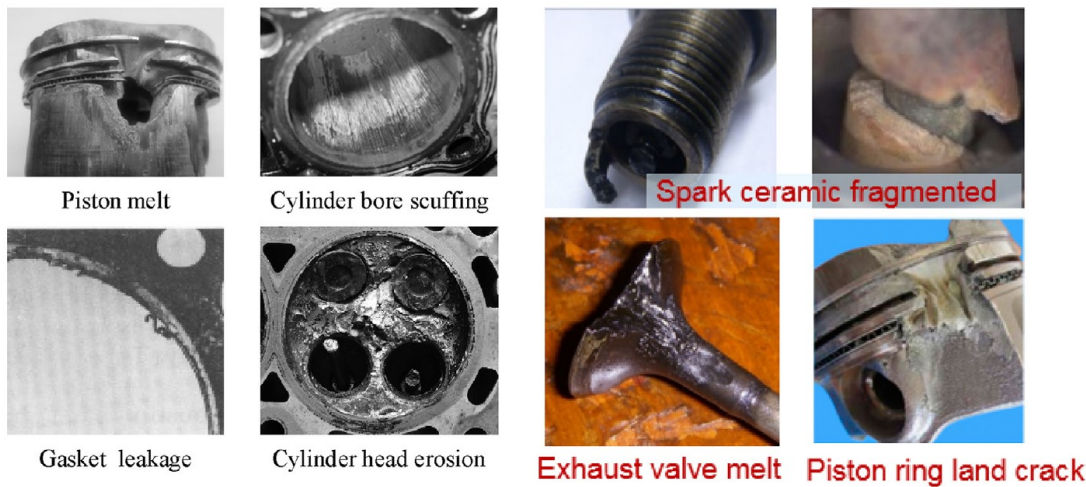
Figure 1.1: Lee Shau Kee Building in which the CCE is located.

Internal combustion engines in today's context Despite the need to reduce greenhouse gas emissions and air pollution, combustion remains the primary source of energy for the World. According to the International Energy Agency [18], in 2020, 70% of the light-duty vehicles and passenger cars will be powered by gasoline engines.

To reduce emissions, governments and international authorities are tightening regulations on internal combustion engines. In the People's Republic of China, according to a recent study from the Ministry of Ecology and Environment, vehicle exhaust emissions represent between 13.5% and 52.1% of the total emissions in 15 of China's largest cities. Such a situation induces important air quality issues. The Chinese government therefore intends to lower its emission rates for domestically produced passenger cars from 5L/100km in 2020 to 3.2L/100km in 2030 [4]. In the European Union, fines on manufacturers may go up to 95€ per CO₂ g/km for each registered vehicle when the vehicle exceeds

the regulation on CO₂ output [5]. To meet with regulations, manufacturers are therefore trying to improve engine efficiency.

Improving gasoline engine efficiency and engine knock To improve gasoline engine efficiency, manufacturers are downsizing engines and using boosters that inject more air into the cylinders. New engines however can malfunction under certain working conditions and suffer severe damage as seen in fig 1.2 [18].



a) Conventional knock (adapted from [1]) b) Super-knock (Reprinted from [2] with permission of SAGE)

Figure 1.2: Typical damage caused by engine knock from Wang et al. [18].

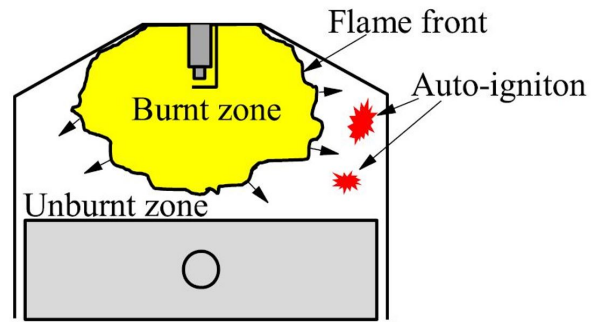
This may occur when, instead of having a propagating flame fully consuming the engine charge, part of the fuel auto-ignites in the combustion chamber. This can cause the cylinder pressure to surge and oscillate (cf fig. 1.3(c)), damaging the engine. The engine noise therefore change, which is why the phenomena is commonly described as "engine knock". These fragmented ignitions can be called "auto-ignitions" or "pre-ignitions" according to the specific way they happen [18].

At random occurrences, the pressure surge from knocking can be particularly strong. This phenomenon, illustrated in figure 1.3(c), is called "super-knock". Scholars are debating the possible conditions under which super-knock may take place [18].

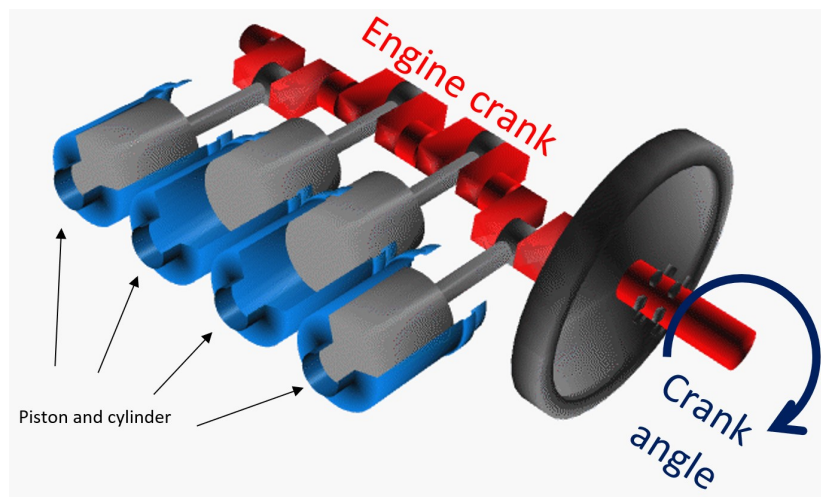
Rapid compression machine experiments to investigate super-knock To study super-knock, researchers at Tsinghua are using an experimental setup called a Rapid Compression Machine (RCM) that imitates the combustion taking place in internal combustion engines [17]. A sketch of the RCM can be found in the appendices figure 7.1.

Inside the RCM's combustion chamber, following the compression phase, a flame is centrally spark-ignited, imitating the main flame inside the cylinder. Due to the isentropic compression of the unburned fuel-air mixture by the flame, a local auto-ignition is taking place at a hot spot. This procedure is employed to imitate a possible pre-ignition due to deposits that formed at the walls of the cylinders.

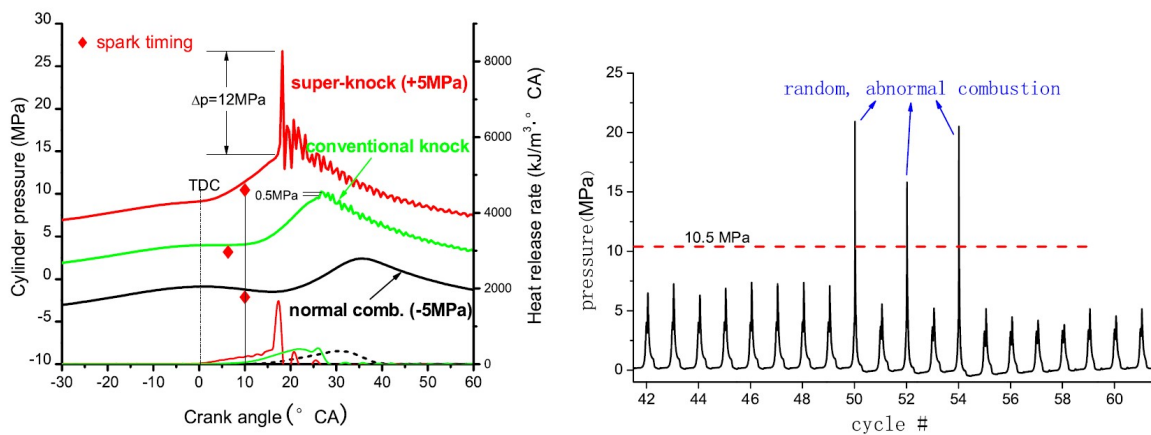
It was found that the interaction between the shock wave generated by the auto-ignition with the main flame/deflagration may cause the rest of the unburned gas to detonate [17]. An illustration of the experiments and the simulations carried out are shown in figure 1.4. Detonation by interaction between the shock wave and the flame may therefore be a possible way to explain the super-knock onset mechanism.



(a) Auto-ignition mechanism from Wang et al. [17]



(b) Description of crank angle [12].

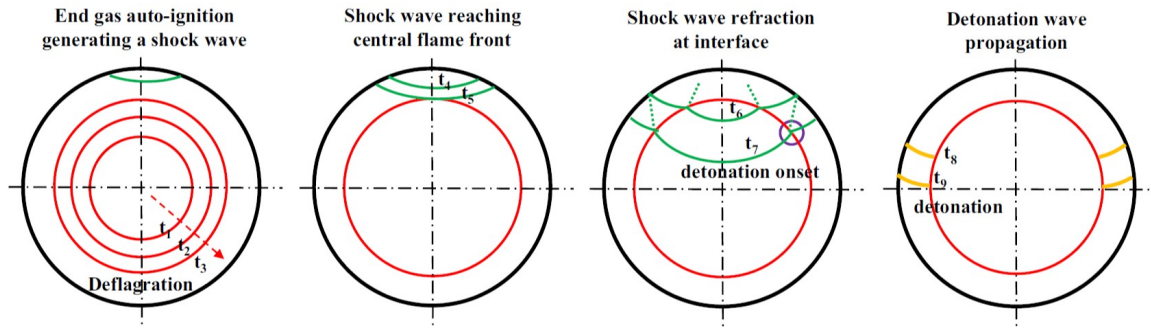


a) Three typical combustion pressures traces

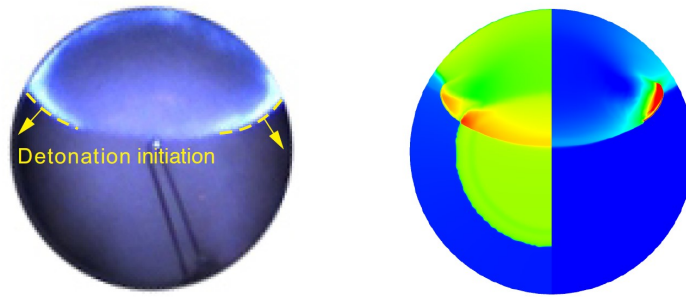
b) continuous engine cycles with random super-knock

(c) Cylinder pressure profile in case of knock [18], description of crank angle from left graph in 1.3(b)

Figure 1.3: Description of engine knock mechanism in internal combustion engines.



(a) Main steps of SWFID induction process from Y. Wang et al [17].



(b) On the left: Picture of an RCM experiment seen through the combustion chamber window; on the right: simulation of the experiment

Figure 1.4: Shock Wave Flame Interaction Induced Detonation (SWFID).

Super-knock and shock wave refraction Because the acoustic impedance in the flame is greater than in the unburned end-gas, the auto-ignition shock-wave is refracted when interacting with the flame. Shock wave refraction theory can therefore be applied to this experimental configuration. The purpose of my internship was therefore to study shock wave refraction at a slow-fast gas interface by using published literature [1, 2, 7, 8, 9, 10, 11, 20, 13] to eventually help develop a theoretical model of the RCM super-knock experiment considering a spherical interface as in the super-knock case.

Matlab code A commented matlab code was developed during this internship for computations and plots. The codes are available on a GitHub project [6].

Chapter 2

Shock wave refraction at a plane interface

Shock wave refraction takes place when the structure of a shock wave changes because it travels through phases with different acoustic impedance, which is the product of the density and the speed of sound. The RCM experiment previously described is an example of shock wave refraction. In the RCM experiment, the shock wave is first propagating through the cool unburned gas before reaching the central flame. Because the central flame is hotter than the unburned gas, the acoustic impedance in the flame is greater than in the fresh unburned gas.

In this section I describe the fundamental aspects of the refraction of a plane shock wave at a plane interface. I will then give in the following chapters a detailed description of shock wave refraction patterns for slow-fast refraction based on past papers to eventually be able to predict which pattern form under specific conditions.

2.1 The plane shock wave refraction fundamentals

Let me detail the fundamentals of shock wave refraction, that will be studied in the following chapter.

Two perfect gas phases I and II are at rest and separated by an interface, m . Each phase has therefore its own ratio of constant heats γ and molar mass \mathcal{M} . The pressure of the gas at rest is written as P_0 . I will first consider that both phases are at same temperature T_0 .

A plane shock wave i , generated in phase I and propagating in a direction normal to itself and a speed W_i , attacks the interface with an angle of incidence noted as ω . Behind the shock, the disturbed gas that has passed through the shock is now at a higher pressure $P_1 > P_0$. We will designate as shock strength the magnitude of the pressure jump which relates to the incident wave's speed.

When the incident shock wave reaches the interface as shown in figure 2.1(b), new compressible-flow waves appear because each gas has a different acoustic impedance, forming what are called shock wave refraction patterns. However, with varying shock strengths χ and varying angles of incidence ω , the refraction systems may change. We may obtain different refraction patterns such as those shown in figure 2.2.

The relative values of $a_{0,I}$ and $a_{0,II}$ strongly influence the configuration of the refraction patterns [9]. If $a_{0,I} > a_{0,II}$, the interface is defined as “fast-slow”. If $a_{0,I} < a_{0,II}$, the interface is defined as “slow-fast”. In the present study, focus was brought on the “slow-fast shock wave refraction” case.

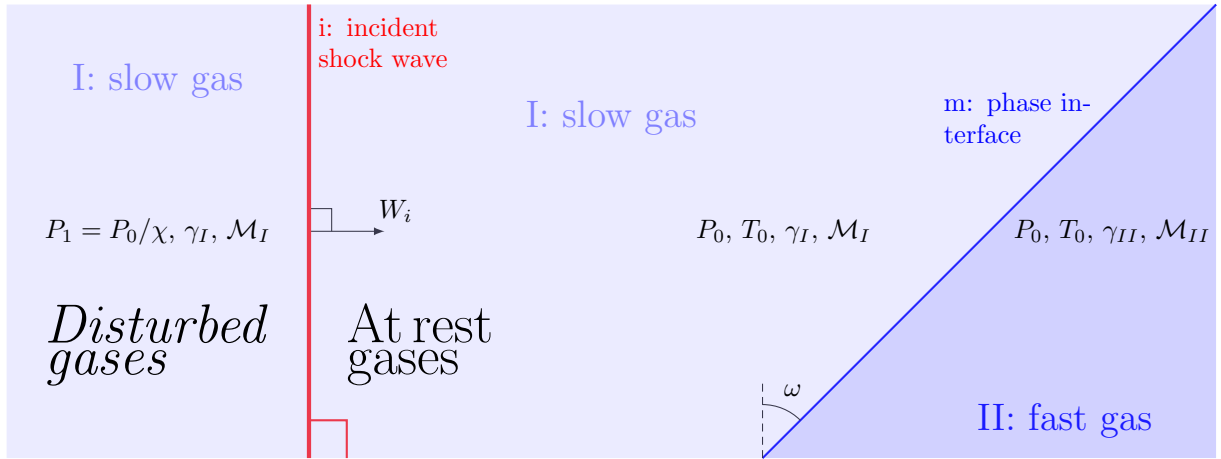
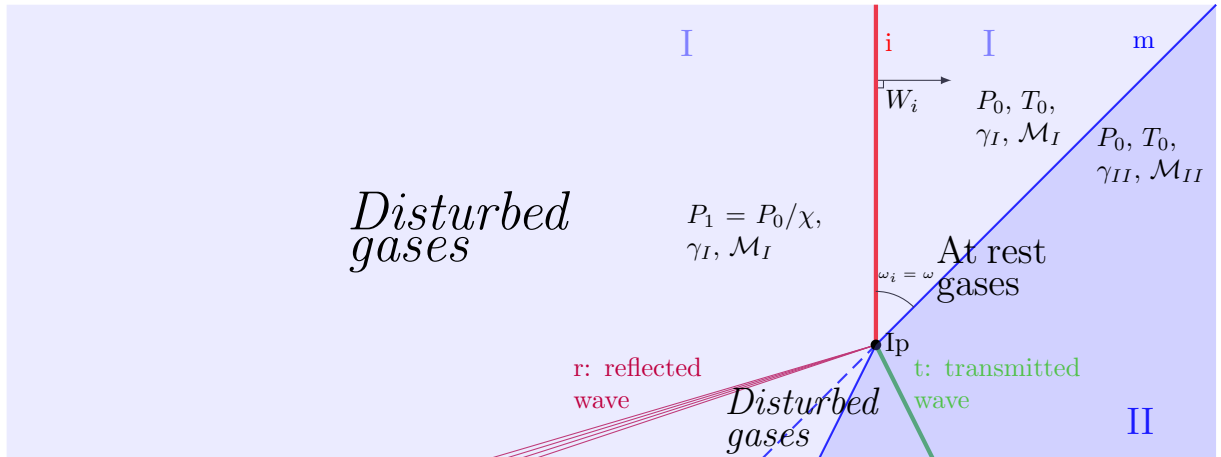
(a) Shock wave moving towards the interface m (b) Example of refraction when shock wave interacts with the interface m

Figure 2.1: Shock wave refraction basic configuration

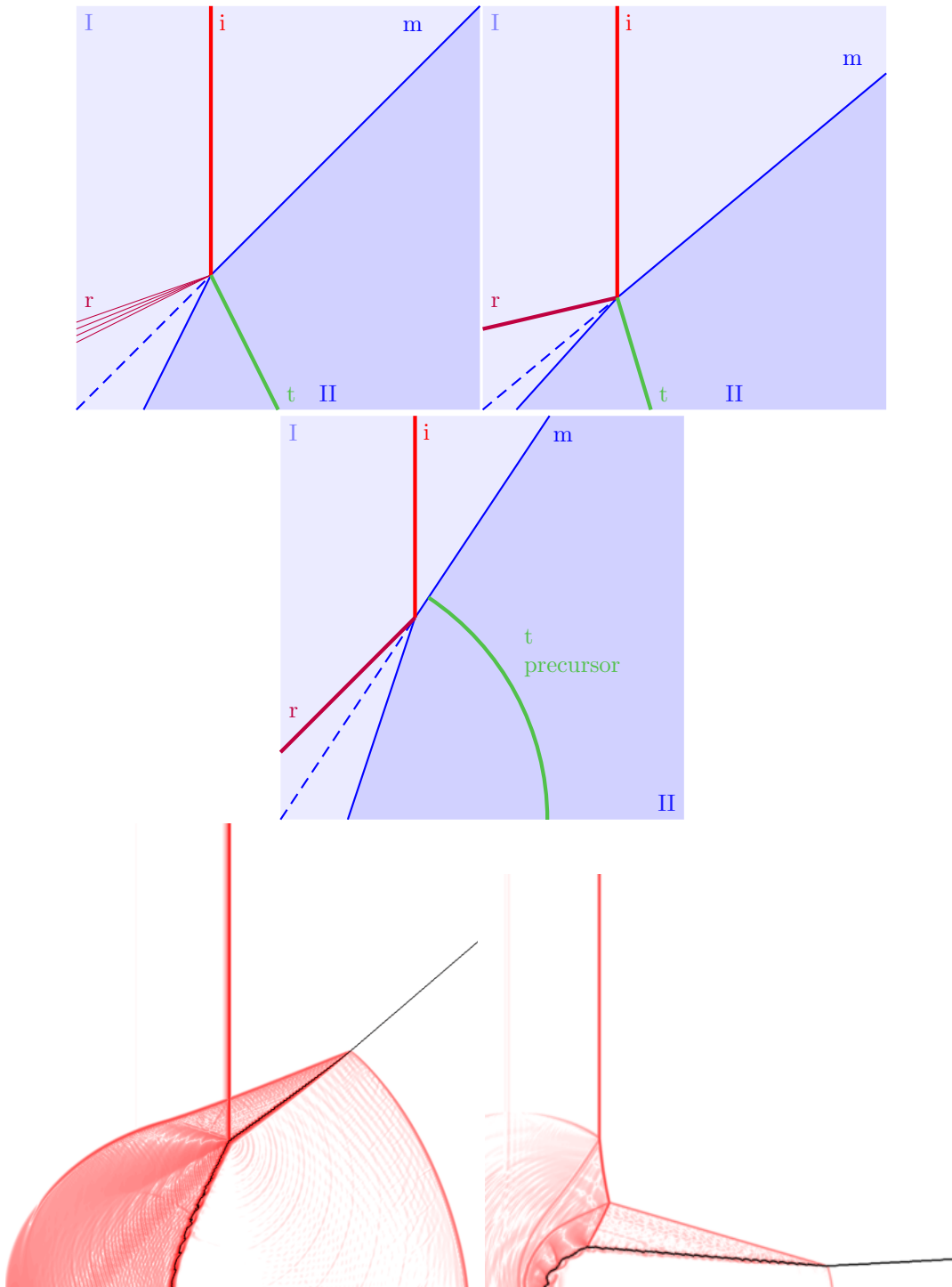


Figure 2.2: Different refraction patterns drawings and finite-element simulation results, courtesy of Gallier.

2.2 Plane shock theory applied to the incident shock wave

The incident shock wave pressure jump is defined as

$$\xi_i = \frac{P_1}{P_0} > 1 \quad (2.2.1)$$

However, for plotting the refraction regime diagram, the inverse of this fraction $\chi = \frac{P_0}{P_1} \in [0, 1]$, which appears in fig. 2.1, will be used. The shock Mach number M_{si} is defined as:

$$M_{si} = \frac{W_i}{a_{0,I}}$$

where $a_{0,I}$ is the speed of sound in the undisturbed gas of phase I . Because the gas is **perfect**, we have that $a_{0,I} = \sqrt{\gamma_I R_I T_0}$ where $R_I = \frac{R_u}{\mathcal{M}_I}$, $R_u = 8.314 \text{ J.K}^{-1}.\text{mol}^{-1}$ is universal perfect gas constant.

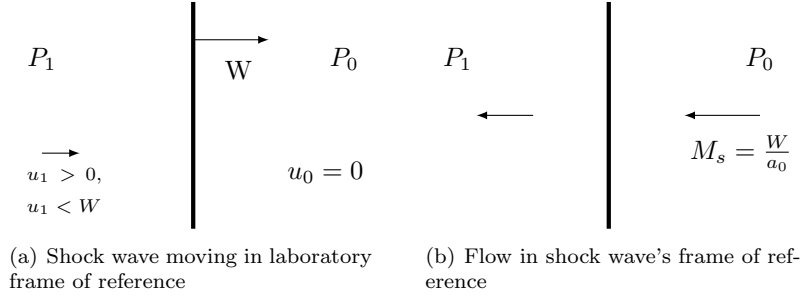


Figure 2.3: Flow directions in the laboratory frame of reference and in a frame of reference moving attached to the plane shock wave

By observing the flow in the frame of reference attached to the shock wave, as shown in fig. 2.3 and using the relation linking pressure jump and Mach number, the following equation is obtained

$$M_{si}^2 = \frac{(\gamma_I - 1) + (1 + \gamma_I)\xi_i}{2\gamma_I}$$

where Mach M_{si} is characterized by ξ_i , so that the shock wave speed W_i is defined in terms of shock strength $\xi_i = 1/\chi$.

As an example, a shock wave of strength $\chi = 0.78$ propagating in CO_2 , with $\gamma_I = 1.288$ and $\mathcal{M}_I = 44.01$, leads to $M_{si} = 1.12$.

Chapter 3

Refraction wave patterns and theoretical models

In this section, the way refraction patterns form for a given angle of incidence ω_i and a given shock strength, defined by ξ_i or χ , will be presented. Geometrical and von Neumann polar analysis will both be employed to explain and interpret these refraction patterns.

The polar analysis will be illustrated by considering refraction at a slow-fast CO_2-CH_4 interface. This example was chosen because it has been previously studied both experimentally, by Abd-El-Fattah and Henderson [1], and numerically by Nourgaliev [13].

3.1 Frame of reference and i polar

To make the polar analysis, the frame of reference attached to Ip will be used. Ip is defined as the point at which the incident shock wave ends; whether it be at the intersection with the interface as in a regular refraction, shown in fig 3.2, or at the intersection with other shock waves propagating in phase *I* for irregular refraction 3.5.

In Ip's frame of reference, the Mach number of the flow before *i* is

$$M_i = \frac{\frac{W_i}{\sin(\omega_i)}}{a_{0,I}} = \frac{M_{si}}{\sin(\omega_i)} \quad (3.1.1)$$

A polar of the incident wave can now be plotted. In the following polar example, see figure ??, phase *I* was CO_2 , $\chi = 0.78$, i.e. $\xi_i = 1.28$, and $\omega_i = 31^\circ$, so that $M_i = 2.2$.

The deviation of the flow behind the *i* wave δ_1 can be deduced from the intersection of the horizontal line for which $\xi = \xi_i$ with the *i* polar. The Mach number after the *i* shock and before the *r* wave M_r [19] is given by

$$M_r^2 = \frac{M_i^2((\gamma_I + 1)\xi_i + (\gamma_I - 1)) - 2(\xi_i^2 - 1)}{\xi_i((\gamma_I - 1)\xi_i + (\gamma_I + 1))} \quad (3.1.2)$$

For this example, $\delta_1 = 4.6^\circ$ and $M_r = 2.0$ are obtained.

3.2 Regular refraction

Regular refraction is a refraction system where Ip is located on the interface and three waves meet at Ip: the incident *i* shock wave in phase *I*, a "transmitted" *t* shock wave in phase *II* and a "reflected" *r* wave in phase *I*.

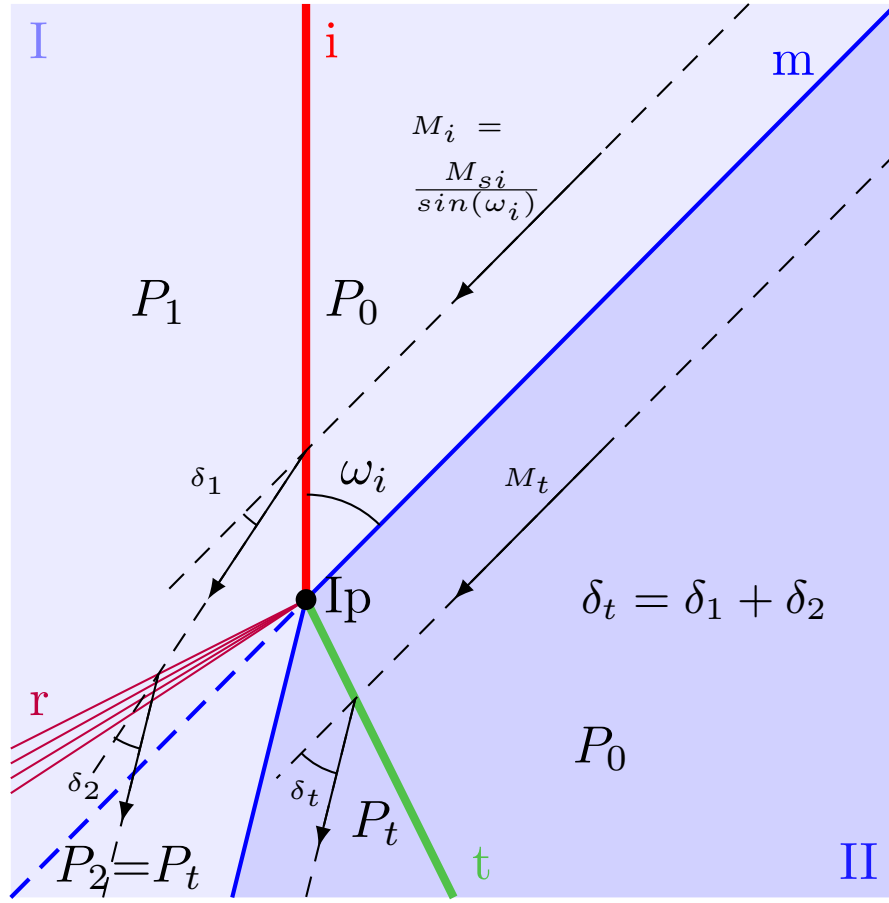


Figure 3.1: Flow description for a Regular Refraction with a reflected Expansion (RRE) in the frame of reference attached to the incident point Ip.

In this section, regular refraction patterns and the conditions under which they may form are investigated. Figure 3.1 shows the flow in the frame of reference attached to the point of incidence in the case of a Regular Refraction with a reflected Expansion (RRE).

3.2.1 t polar

In the Ip's frame of reference, the gas at rest is traveling at the same velocity on either side of the interface. As a consequence, M_t , the Mach number of the flow passing through t is

$$M_t = \frac{a_{0,I}}{a_{0,II}} \cdot M_i \quad (3.2.1)$$

where $a_{0,II}$ is the speed of sound in gas II before the shock.

A transmitted shock wave polar can thus be obtained. Figure 3.2 shows the polar of the transmitted wave propagating in CH_4 with $\gamma_{II} = 1.303$ and $\mathcal{M}_{II} = 16.04$. The transmitted shock Mach number is therefor $M_t = 1.3$.

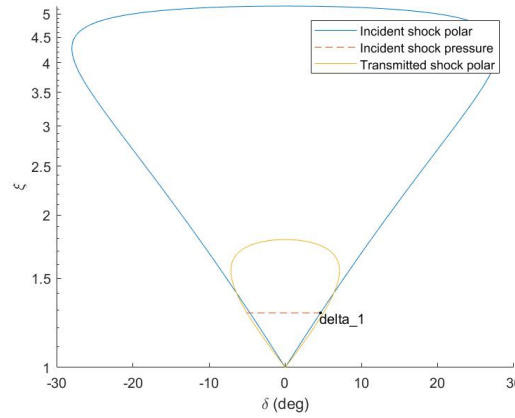


Figure 3.2: Incident and transmitted shock polars for a slow-fast CO_2-CH_4 interface, with $\chi = 0.78$ and $\omega_i = 31^\circ$.

3.2.2 Membrane equilibrium

As seen in fig. 3.1, the flow is deflected twice in phase *I*: first by the *i* wave (δ_1 deflection/deviation), and then by the *r* wave (δ_2 deflection/deviation). In phase *II*, the flow is deviated after crossing the *t* wave (δ_t deviation).

Since the pressure is the same in both phases and the total deviation in phase *I* is the same as in phase *II*,

$$\delta_1 + \delta_2 = \delta_t \quad (3.2.2)$$

and $P_t = P_2$ i.e. $\frac{P_t}{P_0} = \frac{P_2}{P_1} \frac{P_1}{P_0}$, which leads to

$$\xi_r \cdot \xi_i = \xi_t \quad (3.2.3)$$

where $\xi_t = \frac{P_t}{P_0}$, $\xi_r = \frac{P_2}{P_1}$, and $\xi_i = \frac{P_1}{P_0}$

3.3 Regular refraction with a reflected expansion (RRE)

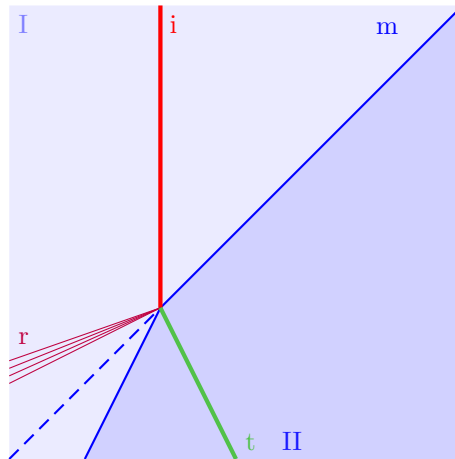


Figure 3.3: Wave pattern for Regular Refraction with a Reflected shock (RRR).

In this situation the reflected wave is an expansion wave as shown in figures 3.1 and 3.3. The pattern is thus called a regular refraction with a reflected expansion (RRE) [1].

Because the gas is perfect, and because the flow going through the expansion wave can be considered as isentropic, the following relationship applies

$$\xi_r = \frac{P_2}{P_1} = \left(\frac{1 + \frac{\gamma_I - 1}{2} \cdot M_2^2}{1 + \frac{\gamma_I - 1}{2} \cdot M_r^2} \right)^{\frac{\gamma_I}{1 - \gamma_I}} \quad (3.3.0.1)$$

where M_2 is the Mach number, downstream of the r wave, in Ip's frame of reference.

According to the theory of Prandtl-Meyer expansions [7]

$$\delta_2 = \nu(M_2) - \nu(M_r) \quad (3.3.0.2)$$

where ν is the Prandtl-Meyer function is given by

$$\nu(M) = \sqrt{\frac{\gamma + 1}{\gamma - 1}} \operatorname{atan} \left(\sqrt{\frac{\gamma - 1}{\gamma + 1}} (M^2 - 1) \right) - \operatorname{atan}(\sqrt{M^2 - 1})$$

where $\gamma = \gamma_I$.

Equations 3.3.0.1 and 3.3.0.2 are sufficient to calculate the pressure drop through the expansion as a function of the deviation on the polar diagram.

By starting the $\delta - \xi_i$ plot for the expansion at the (δ_1, ξ_i) , and thanks to equations 3.2.2 and 3.2.3, it is found that (δ_t, ξ_t) is at the intersection of the expansion plot with the t polar.

From fig. 3.4, it is found for the CO_2-CH_4 example that $\delta_t = 4.8^\circ$ and that $\xi_t = 1.27$.

In some cases where the reflected wave can be a shock wave or an expansion wave, multiple solutions exist. However, experiments point out that only the weaker solutions with expansions physically take place [10].

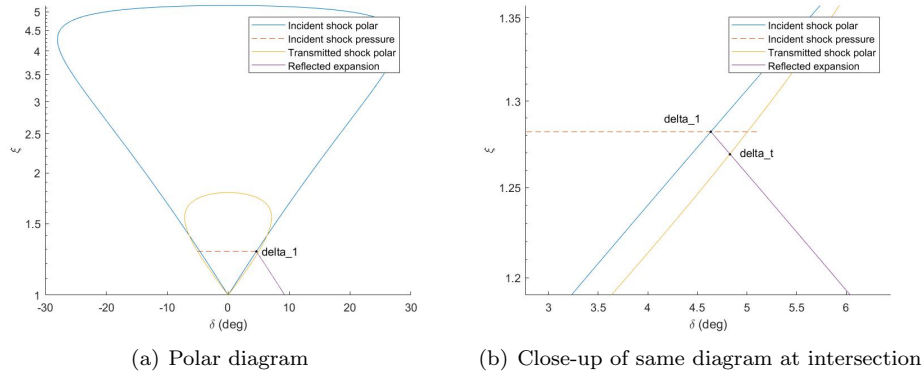


Figure 3.4: Polar diagram for RRE patterns.

3.3.1 Transition from reflected expansion to reflected shock

As will be explained later, when solutions with expansion waves no longer exist, there are regular refraction patterns where the reflected wave is a shock wave. The conditions for which the transition from expansion fan to shock wave takes place are further discussed.

As the reflected wave becomes a Mach line, inducing no pressure jump or flow deviation, as illustrated in fig.3.5, equations 3.2.2, and 3.2.3 become [8]

$$\delta_1 = \delta_t \quad (3.3.1.1)$$

$$\xi_t = \xi_i \quad (3.3.1.2)$$

Therefore an analytical resolution of this transition boundary at given ξ_i and given ω_i can easily be computed.

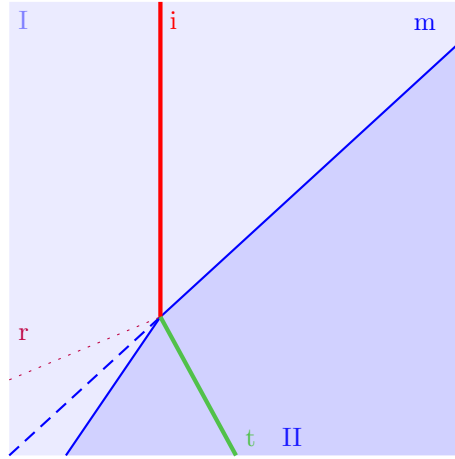


Figure 3.5: Transition from a regular refraction with a reflected expansion to a regular refraction with a reflected shock. In this case, r corresponds to a Mach line.

3.4 Regular refraction with a reflected shock (RRR)

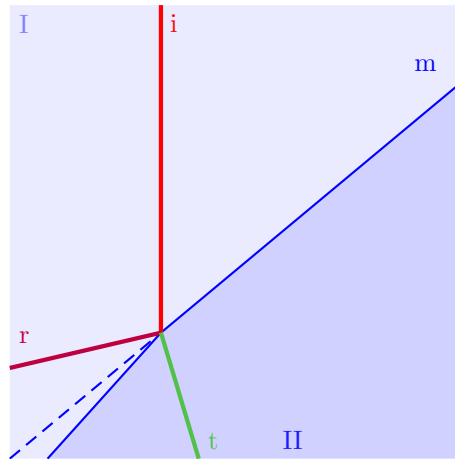


Figure 3.6: RRR refraction

In this case, the refraction pattern is called a Regular Refraction with a Reflected shock (RRR) [1], illustrated in figure 3.6.

As explained in 3.1, for given ξ_i and ω_i , the Mach number before the reflected wave M_r can be obtained, and thus, the reflected shock polar can be plotted. Similar to the approach employed in the previous section 3.3, the pressure and deviation downstream of the refraction system can be obtained from the intersection of both polars by starting the t-polar plot at (δ_1, ξ_i) . Analytical solutions can also be found and take the form of a polynomial equation of degree 12 [9].

This leads to two intersections, i.e. two possible solutions, but the physically observed solution is always the weakest solution.

Figure 3.7 shows the polars for an incident shock of strength $\chi = 0.8$, and angle of incidence $\omega_i = 33.8^\circ$, at a CO_2-CH_4 interface.

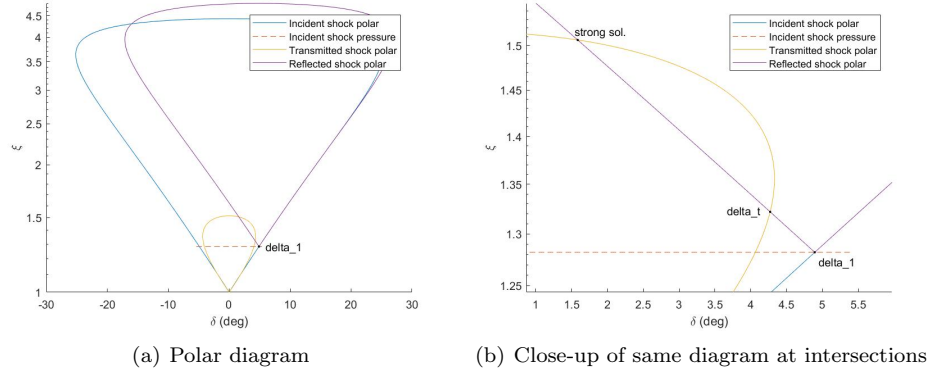


Figure 3.7: Polar diagram for RRR at a slow-fast CO_2-CH_4 interface.

3.4.1 Transition from regular refraction to irregular refraction

As seen in figure 3.8, at constant χ and as ω_i is increased, the reflected wave polar will eventually become tangent to the t-wave polar, therefore making the membrane equilibrium impossible for greater angles of incidence. The regular refraction systems are therefore no longer possible and new refraction patterns called "irregular refraction" patterns will appear [1].

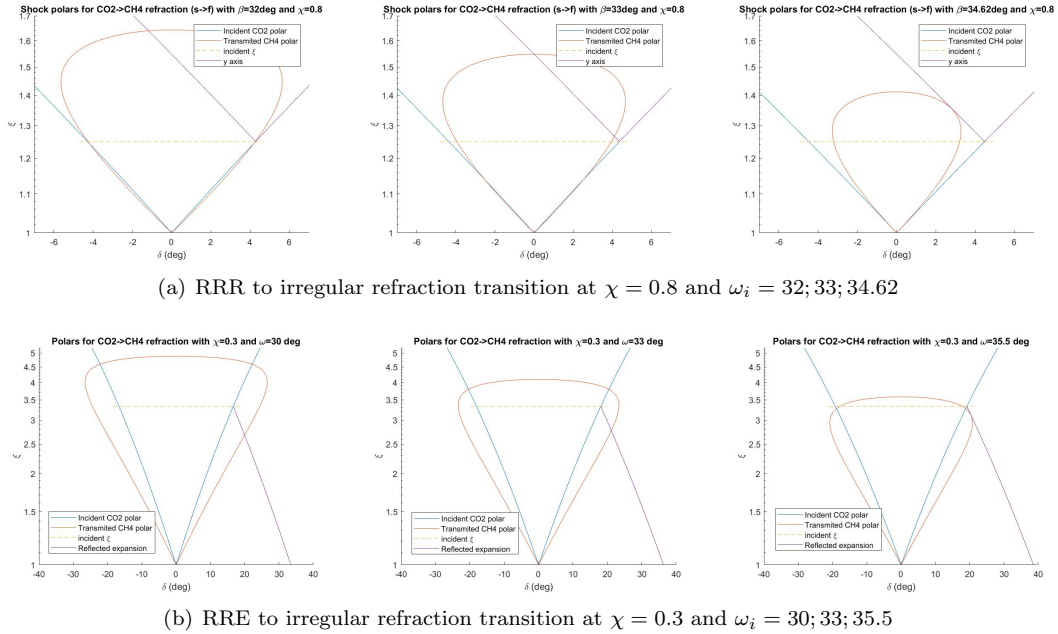


Figure 3.8: Polar diagrams for transition from regular to irregular refraction at a slow-fast CO_2-CH_4 interface.

3.5 Irregular refraction patterns

The irregular refraction patterns as well as conditions for which transition between the different structure are taking place are now discussed. Irregular refraction patterns appear when regular refraction patterns are no longer possible. The transmitted shock wave now moves ahead of the incident wave and is described as a “precursor” wave [2].

When the transmitted wave moves approximately at the speed of the incident wave it is called a “bound precursor”, as will be detailed in section 3.5.1. Otherwise, when the transmitted wave moves faster than the incident wave, it is called a “free precursor”, as will be seen in section 3.5.3. When the ω angle of incidence is sufficiently large, a Mach stem appears in the pattern, as explained in section 3.5.6.

3.5.1 Piston theory to estimate precursor t-wave speed

Abd-El-Fattah et al. [2] detail a “piston theory” to estimate the normal speed of the transmitted wave W_t when knowing the incident wave’s speed W_i :

$$W_t = \frac{1}{2} (b + \sqrt{b^2 + 4a_{0,II}^2}) \quad (3.5.1.1)$$

where b is given by

$$b = \frac{\gamma_{II} + 1}{\gamma_I + 1} \frac{W_i^2 - a_{0,I}^2}{W_i} \quad (3.5.1.2)$$

3.5.2 Bound Precursor Refraction (BPR)

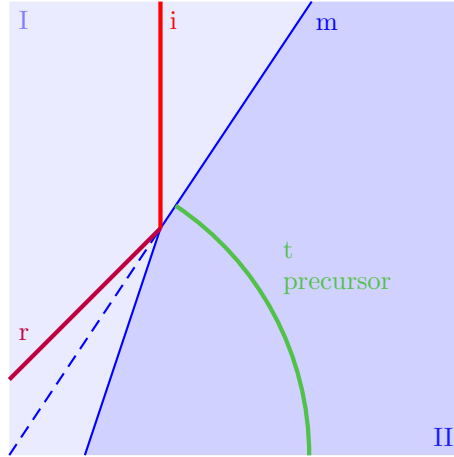
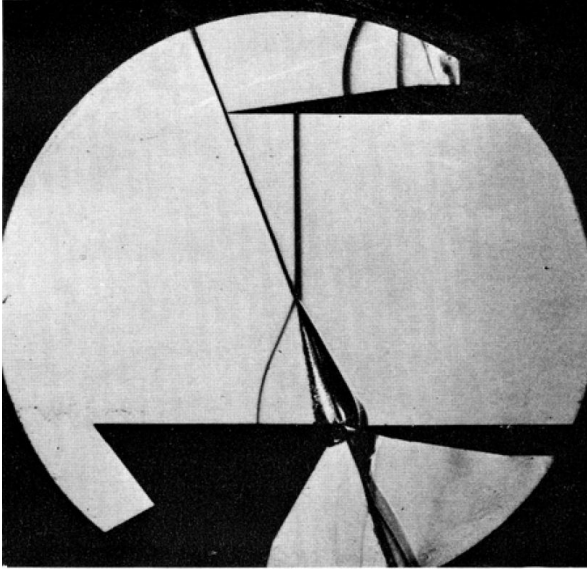


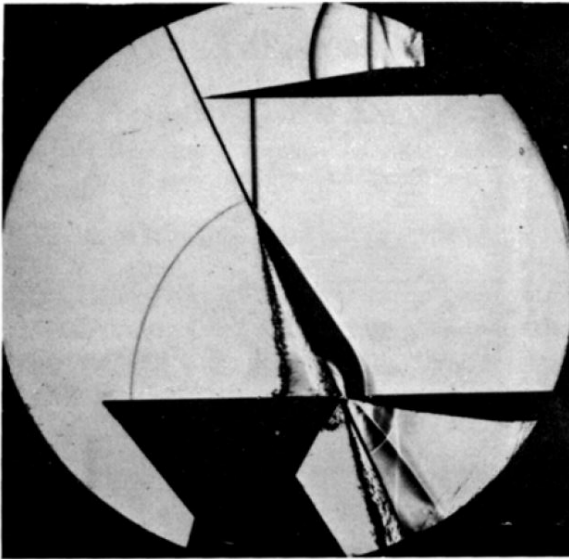
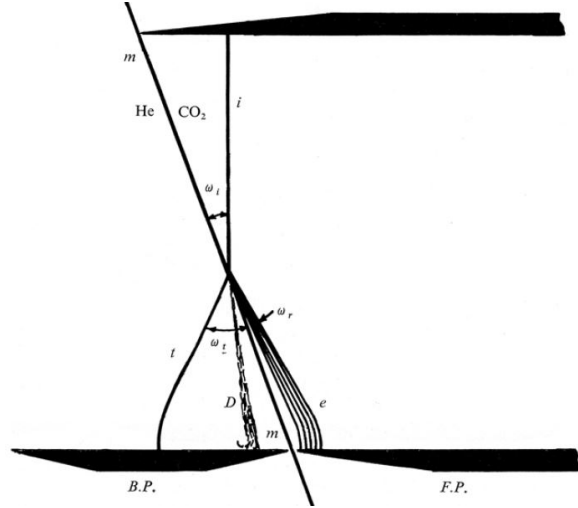
Figure 3.9: Structure of a Bound Precursor Refraction (BPR)

The first irregular pattern that appears when increasing ω at constant χ is called Bound Precursor Refraction (BPR) [1] as shown in figure 3.9. The term “bound” comes from the fact that the transmitted wave is not yet moving faster than the incident wave as it is the case in other patterns.

Because the transmitted shock moves at the same speed, BPR patterns can look very similar to regular patterns. The BPR pattern is different in that the transmitted wave is slightly ahead of the incident wave as observed experimentally [2]. This is shown in fig 3.10.



(a) RRE pattern



(b) BPR pattern

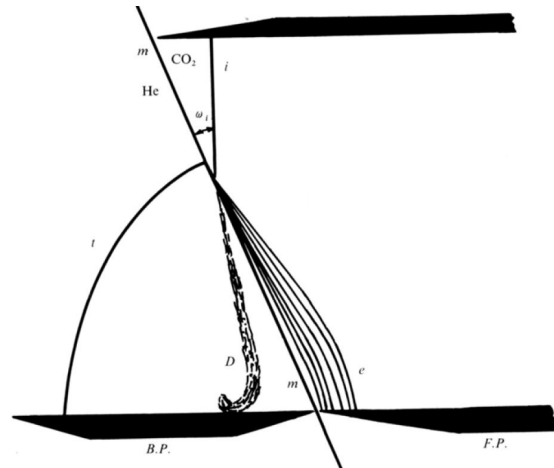


Figure 3.10: RRE and BPR patterns obtained in Abd-El-Fattah et al. [2] experiments.

3.5.3 Transition from bound precursor to free precursor refraction

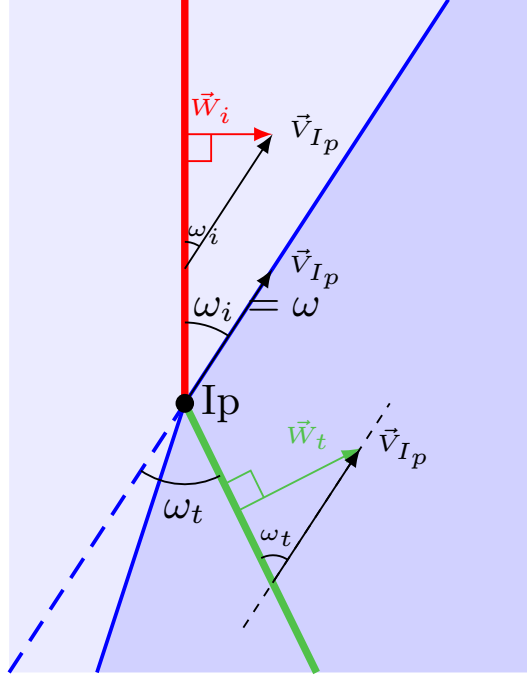


Figure 3.11: Incident and transmitted wave speeds when transmitted wave is bound, here in the case of regular refraction

As the angle of incidence is further increased, the BPR pattern may transit to another irregular pattern.

As illustrated in figure 3.11 since the transmitted shock and the incident shock move at the same speed, their angles of inclination, ω_t and ω_i , as well as their normal speeds in the laboratory frame of reference, W_t and W_i , have to verify the following equation

$$\frac{W_i}{\sin(\omega_i)} = \frac{W_t}{\sin(\omega_t)} = V_{Ip} \quad (3.5.3.1)$$

Because $\sin(\omega_t) \in [0, 1]$, this condition can no longer be satisfied when

$$\sin(\omega_i) \frac{W_t}{W_i} > 1$$

According to the piston theory equation 3.5.1.1,

$$M_{st} = \frac{1}{2}(c + \sqrt{c^2 + 4})$$

where M_{st} is transmitted shock Mach number and

$$c = \frac{\gamma_{II} + 1}{\gamma_I + 1} \left(\frac{a_{0,I}}{a_{0,II}} \right)^2 \frac{M_{si}^2 - 1}{M_{si}}$$

Therefore, the “bound transmitted wave condition”, equation 3.5.3.1, transitions at

$$\omega = \omega_F = \arcsin\left(\frac{M_{si}}{M_{st}} \frac{a_{0,I}}{a_{0,II}}\right) \quad (3.5.2)$$

For $\omega > \omega_F$, the t wave is no longer bound, i.e. not moving at the same speed as the incident shock. The transmitted wave is then described as a “free precursor”.

3.5.4 Free precursor patterns

Henderson et al. [1, 2, 9, 10] describe a range of irregular patterns with free precursors. Among them are the Free Precursor von Neumann Refraction (FNR), and the Free Precursor Refraction (FPR).

***j* and *k* waves** For free precursor patterns, a new shock appears to link the transmitted wave to the incident shock. This wave is referred to as the *j* wave (see figs. 3.12, 3.14(a)).

Behind the *j* wave, another wave called “*k* wave” appears between the *m* interface and *Ip*. *Ip* is now moving along the (LIp) line. Because the flow speed behind *k* can differ from the flow speed behind *r*, a slip surface forms (SS in fig 3.12).

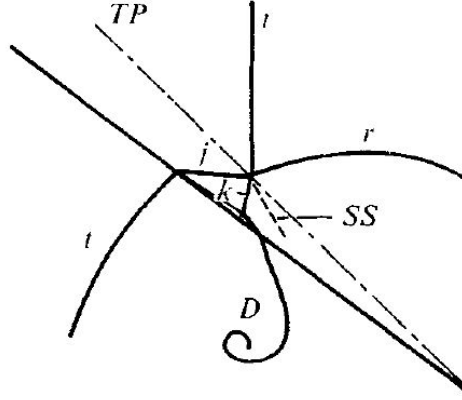


Figure 3.12: Drawing from Abd-El-Fattah and Henderson showing *j* and *k* waves [1]

Definition of the new angles New angles now have to be defined to describe the geometry of the free-precursor patterns. These angles, ω_i and Δ , are shown in figure 3.14(a). ω_i remains the angle between (LIp) and the *i* wave. δ is the angle between the at rest interface and (LIp)

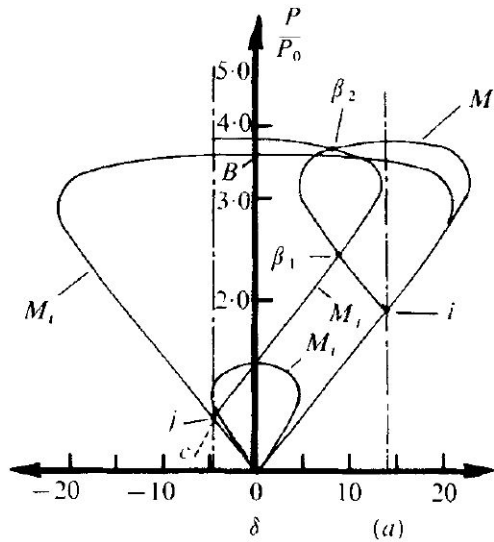
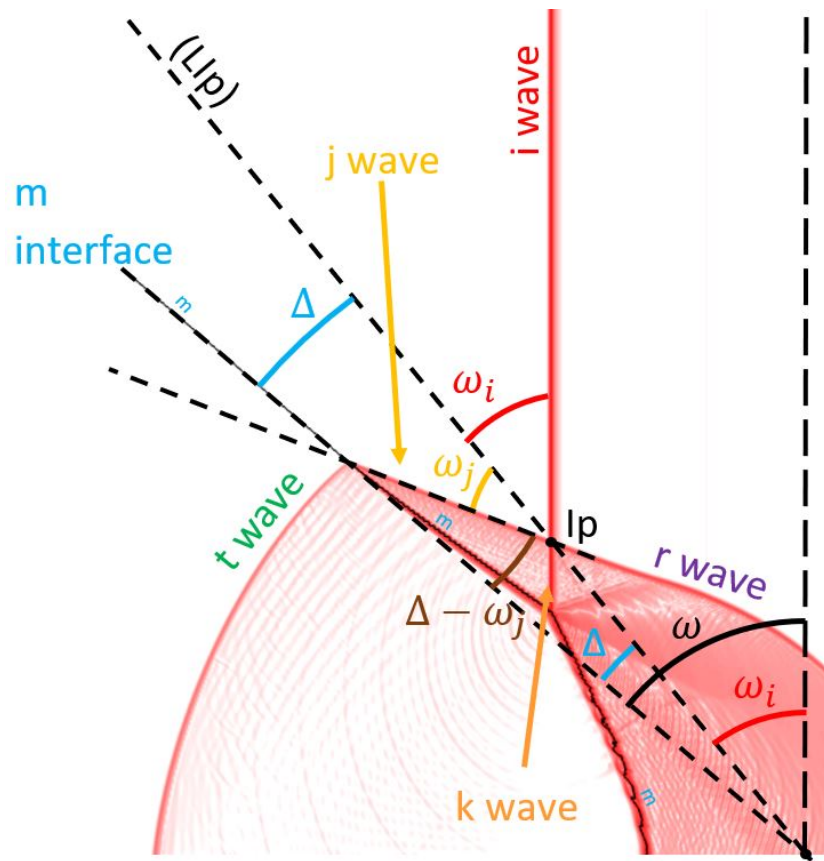
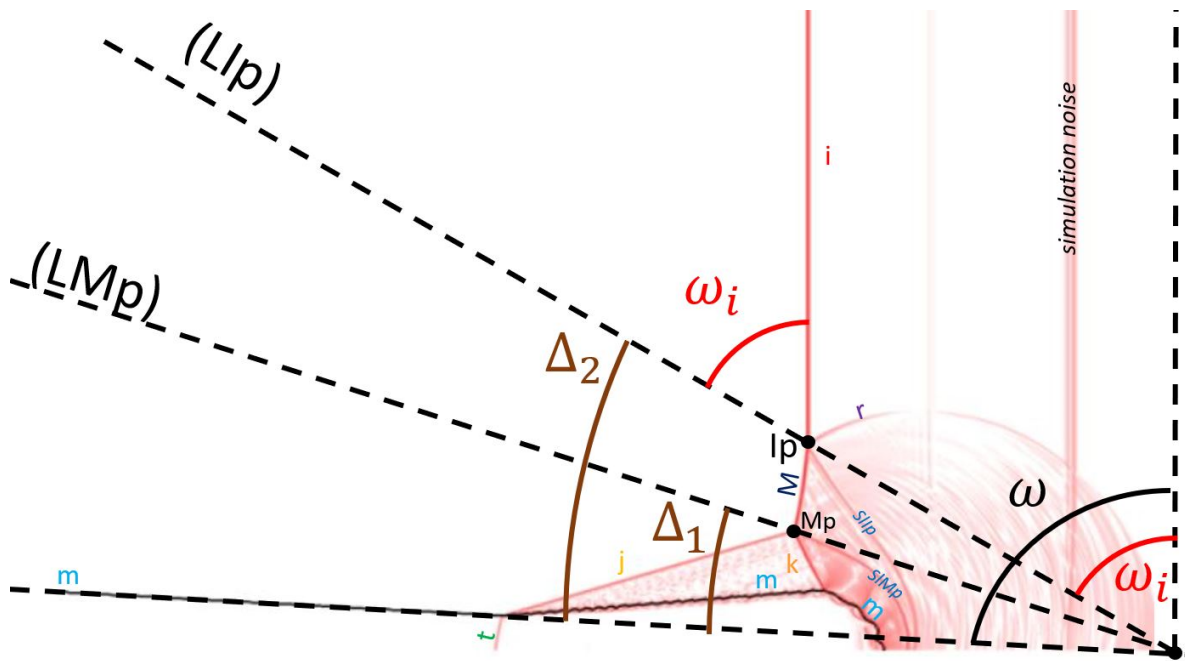


Figure 3.13: Polar diagram with free precursor from Abd-El-Fattah and Henderson [1].



(a) Simulated shock wave refraction with a free precursor



(b) Simulated shock wave refraction with a Mach stem

Figure 3.14: Examples of numerical Schlieren of refraction with free precursors, courtesy of Gallier.

j and k polars j and i are both described by the same polar because the j wave intersects with the i wave and because both are in phase I .

Similar to the r wave in RRR refraction (see section 3.4), the k wave polar starts from a point on the i - j polar. Also to the regular refraction case (see 3.2), the flow behind the k wave must have the same pressure and deviation as behind the r wave. If not so, a Mach stem will be formed, as shown in fig 3.14(b).

Without the presence of a Mach stem, the refraction system is therefore at the intersection of the k and the r polar. A polar diagram example is given in figure 3.13.

3.5.5 Computing the k wave polar

The j wave's shock Mach (M_{sj}) is estimated by using a well-known shock-tube equation giving the shock Mach of a wave generated by a membrane separating gases with different pressures

$$\frac{P_t}{P_0} = \frac{1 - \gamma_I + 2\gamma_I M_{sj}^2}{\gamma_I + 1} \left(1 - \frac{\gamma_{II} + 1}{\gamma_I + 1} \frac{a_{0,I}}{a_{0,II}} \left(M_{sj} - \frac{1}{M_{sj}} \right) \right)^{\frac{-2\gamma_{II}}{\gamma_{II} - 1}} \quad (3.5.5.1)$$

In addition,

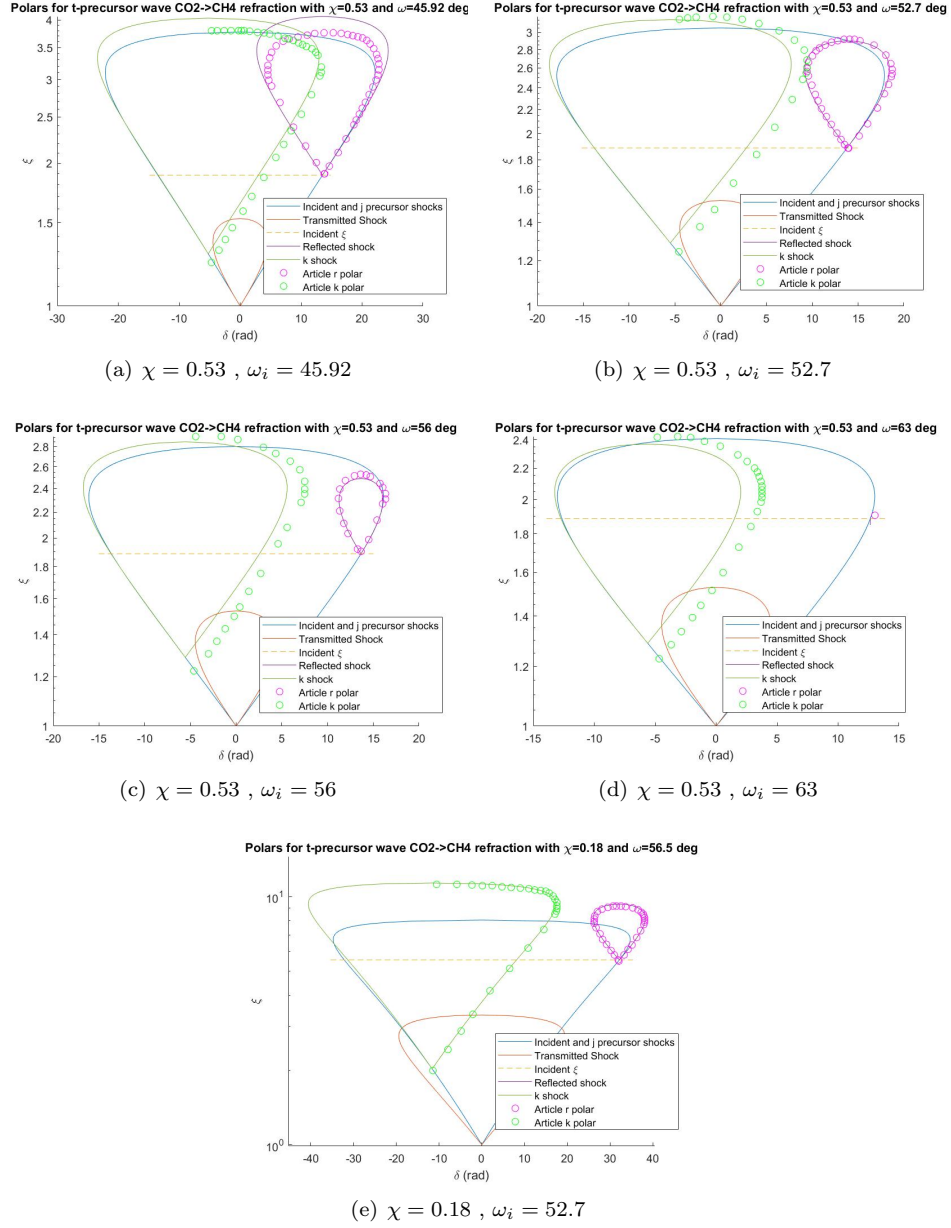
$$\frac{P_t}{P_0} = \xi_t = \frac{1 - \gamma_{II} + 2\gamma_{II} M_{st}^2}{\gamma_{II} + 1}$$

where M_{st} is the transmitted shock Mach number. It is computed using piston theory as done in the BPR section 3.5.3.

Once M_{sj} is obtained, the ξ_j pressure jump can be computed, and therefore the k polar and its starting point.

Discrepancies with article plots The obtained pressure jump and polars do not exactly correspond to the ones presented in Abd-El-Fattah and Henderson [1]. This is evidenced in fig 3.15. Such a mismatch results in a discrepancy when trying to recover the FPR to TNR boundary as done by Abd-El-Fattah and Henderson, see section 4. The k wave starting points are generally weaker in the papers.

This may be due to the effect of the membrane inertia which Abd-El-Fattah and Henderson took into account in their calculations [2].



3.5.6 Mach stem refraction

Appearance of a Mach stem As explained in the previous section, the $i-r-j-k$ meeting point exists when the k and r wave polars intersect each other. When this is no longer the case as in 3.15(e), a Mach stem appears, splitting the $i-r-j-k$ into two triple points, Ip and Mp, as shown in fig 3.14(b). This happens when ω is sufficiently large.

Abd-El-Fattah and Henderson describe two patterns with Mach stems including TNR (Twin von Neumann Refraction) and TMR (Twin Mach Refraction) [1]. The flow behind the mach stem for the TNR is subsonic and supersonic for the TMR.

Points Ip and Mp respectively move along the lines (LIp) and (LMp). Behind each triple point, because of differences in flow speed, slip lines appear (see SLIp and SLMp in fig. 3.14(b)).

New angles New angles such as ω_i , Δ_1 , Δ_2 can be defined to describe the refraction pattern with Mach stem.

3.5.7 Lambda shock refraction

Lambda shock refraction pattern Abd-El-Fattah and Henderson [1] finally mention the discovery of another refraction pattern, called the Lambda Shock Refraction pattern (LSR). In this pattern, the reflected shock wave seems to have disappeared, with the flow behind the incident wave becoming subsonic as can be seen in fig. 3.16.

Condition for transition to LSR The condition for the transition to LSR can be established by considering the wave pressure jump ξ_i and the ω_i angle (see fig. 3.14(b)).

Because the transition occurs when the r polar reaches the sonic point, i.e. when the flow behind the i wave becomes subsonic, i.e. $M_r = 1$, the following relationship applies

$$1 = \frac{M_i^2((\gamma_I + 1)\xi_i + (\gamma_I - 1)) - 2(\xi_i^2 - 1)}{\xi_i((\gamma_I - 1)\xi_i + (\gamma_I + 1))} \quad (3.5.7.1)$$

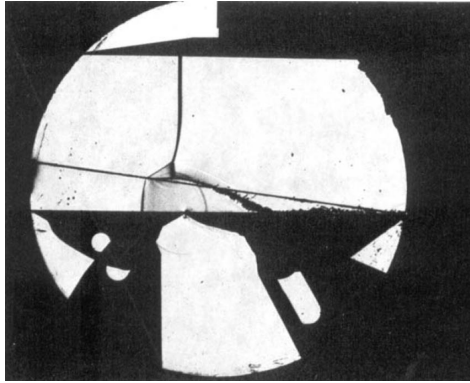


Figure 3.16: LSR pattern photograph [1]

Chapter 4

Refraction regime diagram in ω_i - χ plane

As done by Abd-El-Fattah and Henderson, it was attempted to recompute the refraction pattern boundaries in the ω_i - χ . This corresponds to establishing a regime diagram for the refraction phenomenon. ω_i should not be confused with the ω angle of incidence (see fig. 2.1(a)) because they are not always equal to each other. ω_i is the angle between the incident shock and the trajectory path of I_p (cf. figs 3.3, 3.9, 3.14(a), 3.14(b)).

To confirm the previously established methodology, boundaries were computed for a CO_2 - CH_4 slow-fast interface, and compared to the literature data. The methodology was then transposed to an Ar - He interface, and confronted to finite element simulations.

4.1 Refraction regime diagram for a CO_2 - CH_4 slow-fast interface

To validate the methodology previously presented to calculate the slow-fast refraction pattern boundaries, it was applied to the CO_2 to CH_4 case studied in previous articles [1, 11, 13]. The comparison is shown in fig. 4.1. Along with the computed boundaries, were added the Abd-El-Fattah and Henderson boundaries, as well as points representing the simulations of Nourgaliev et al. [13]. The "FPR to TNR" boundary represents the appearance of a Mach stem.

Discussion For most cases, except for the boundary signifying appearance of a Mach stem, the pattern boundaries from Abd-El-Fattah and Henderson were successfully reproduced. The discrepancy for the FPR-TNR boundary is due to the difference in the calculated k wave polar previously mentioned.

The simulation results from previous articles correspond to the patterns predicted with the theory, but they do not enable to test the theoretical boundaries.

A way of computing the FPR to TNR boundary has been proposed in [20]. Future work will focus on applying this alternative approach.

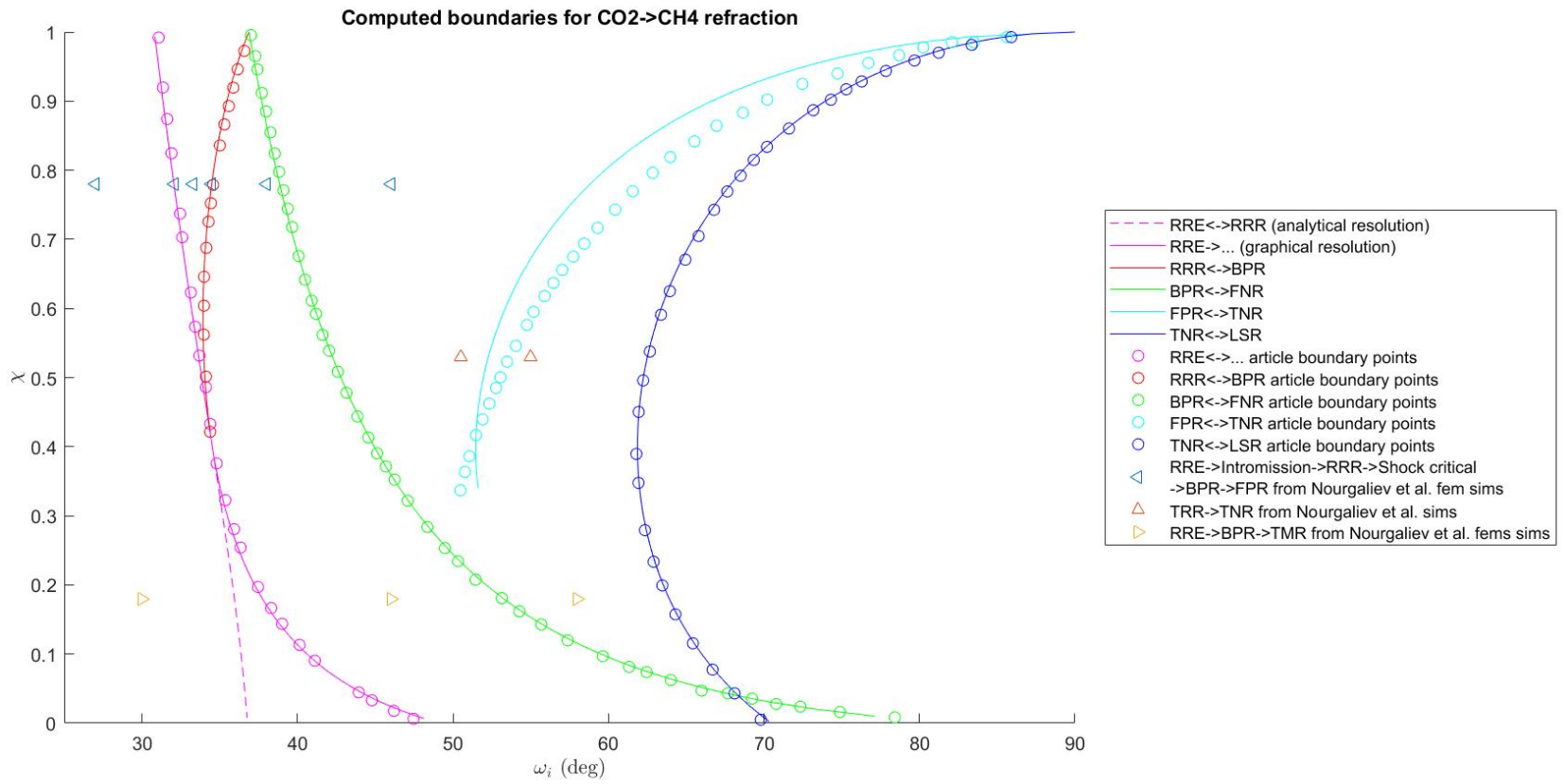


Figure 4.1: CO₂ to CH₄ refraction pattern boundaries

4.2 Refraction regime diagram for a *Ar-He* slow-fast interface

The methodology used to plot the pattern boundaries for the CO_2-CH_4 interface was transposed to the *Ar-He* interface case. This example was chosen because the perfect gas assumption is strictly valid for these gases, and their heat ratios γ are constant. The values of the different gas parameters are described in table 4.1.

Parameter	Value
γ_I	5/3
γ_{II}	5/3
\mathcal{M}_I	40 g/mol
\mathcal{M}_{II}	4 g/mol

Table 4.1: Parameters for refraction at a *Ar-He* interface.

Comparison with finite element simulations Finite element simulations of the different cases were performed by a collaborator (Dr. Stany Gallier from ArianeGroup) to test the validity of the boundaries. The identification of the pattern was performed by Dr. Gallier. To obtain coherent results, Nourgaliev et al. used an adaptive mesh with a peak resolution of $H/800$ [13], where H is the simulation domain height. In the present simulation work, a non-adaptive resolution of $H/2000$ was adopted. An example of simulation obtained for the *Ar-He* interface is shown in 4.2.

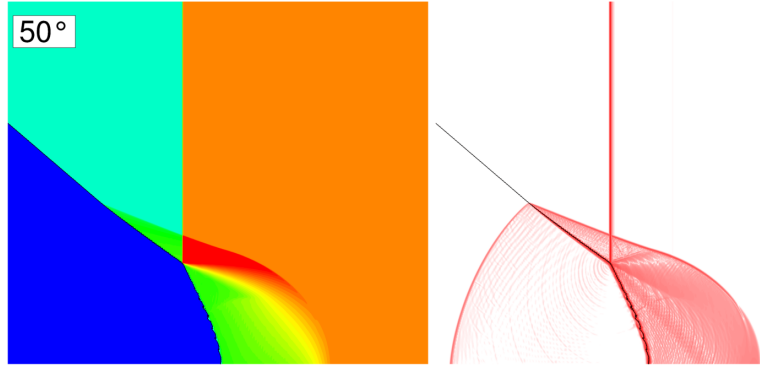


Figure 4.2: Finite element simulation example of the *Ar* to *He* case, courtesy of Gallier. On the left: density field, on the right: schlieren image

Discussion Fig. 4.3 shows how the simulation results overlay with the theoretical pattern boundaries. The boundaries seem to give a reasonable prediction of the patterns for the cases that were tested. The prediction of pattern transition seems to deteriorate as the incident shock gets stronger. Some of the discrepancies may also be explained by the difficulty in unambiguously identifying the refraction patterns.

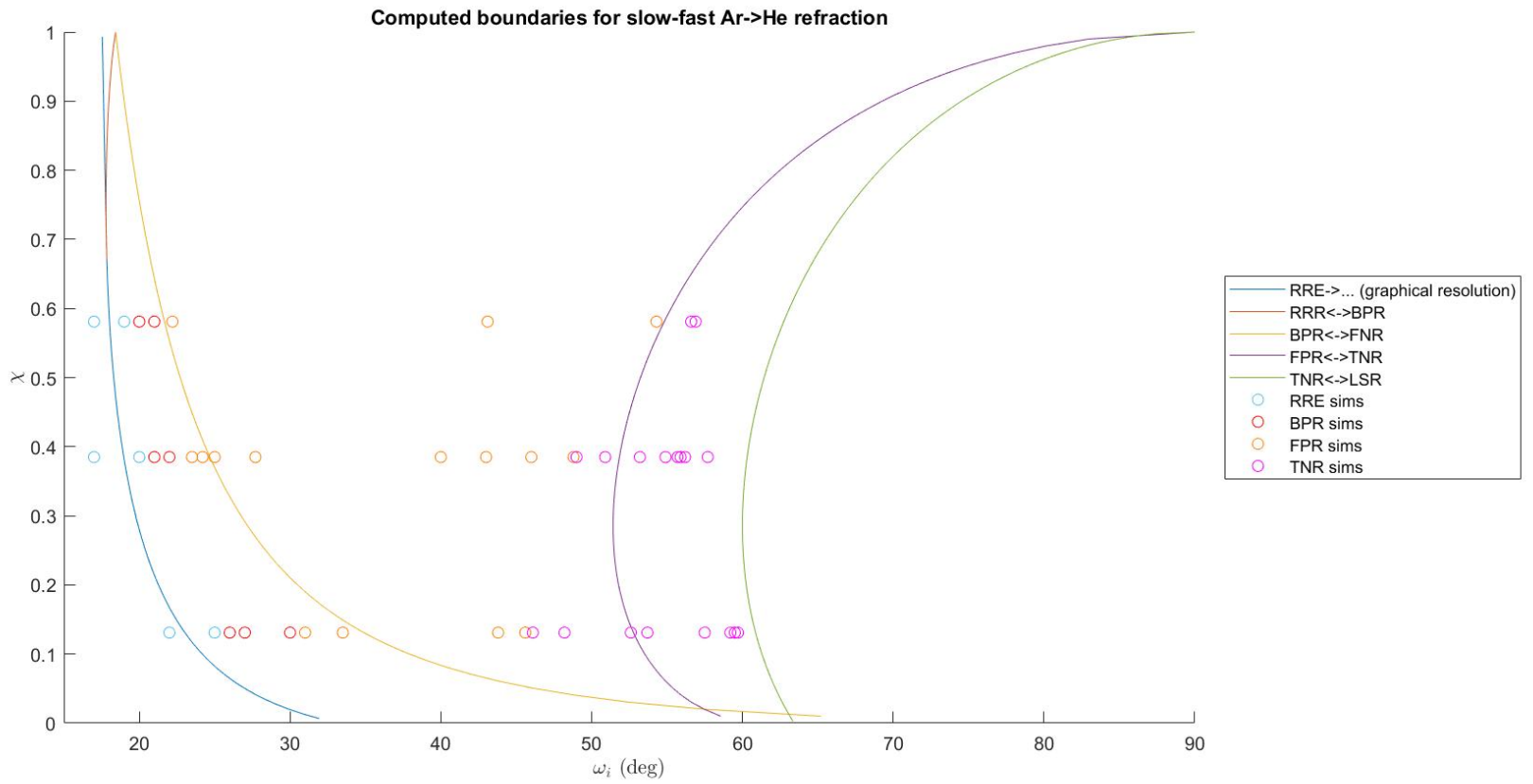


Figure 4.3: Theoretical refraction pattern boundaries for an *Ar-He* slow-fast interface along with points obtained from numerical simulation.

- **RRE to BPR transition:** A few RRE points were identified beyond the "RRE->..." boundary with the simulation vs boundary discrepancy increasing as the incident shock becomes stronger. As explained in section 3.5.1, RRE and BPR patterns can have subtle differences, which may blur the transition limit according to the way the patterns are identified.
- **BPR to FNR transition:** A few FNR points were identified before the "BPR->FNR" boundary with increasing discrepancy as the incident shock gets stronger. Patterns for which the measured Δ angle (see fig. 3.14(a)) was on the order of 1 *deg* were identified as FPR. These patterns have precursors moving at approximately the same speed as the incident, which could make it a "bound precursor". The appearance of a *j* wave and the fact that the precursor becomes free are two possible ways of defining the transition.
- **FPR to TNR transition:** The strongest discrepancies were found at this boundary. Abd-El-Fattah have shown in previous articles that piston theory fails to predict the t wave speed at greater angles of incidence (cf fig. 4.4).
- **LSR transition:** No LSR pattern has been identified. There were no examples of the LSR pattern in the two previous articles on finite-element simulations of slow-fast refraction [13, 11]. This is maybe because reflected Mach waves are identified as shock waves in the numerical schlieren images.

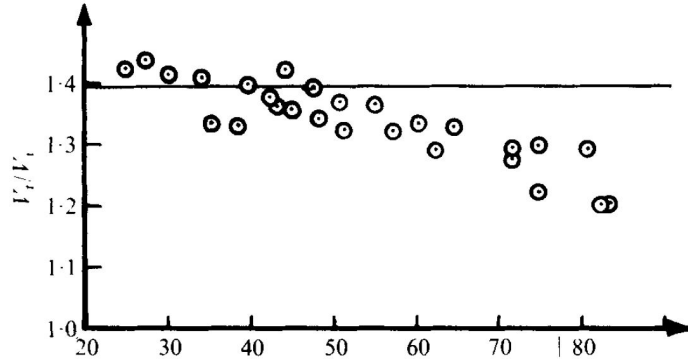


Figure 4.4: W_t/W_i ratio plotted according to the angle of incidence in the case of CO_2 to CH_4 refraction at $\chi = 0.53$ [1]. Line: theoretical value, points: measured value.

Chapter 5

Shock wave refraction at an inert-reactive interface

In order to get closer to the RCM experiment described in the introduction, a shock wave refraction at an inert-reactive interface was considered. The chosen example was for an interface constituted of a cold hydrogen and oxygen stoichiometric mixture and hot helium. The cold $2H_2+1O_2$ phase is a surrogate of the unburned end-gas in the RCM and the hot He is a surrogate of the hot flame products.

To model reactive cases, thermodynamic properties of Lagrangian particles for RRE patterns were computed.

5.1 Refraction regime diagram at a $2H_2+1O_2$ - He interface

The calculated pattern boundaries for refraction from cold $2H_2+1O_2$ to hot He are shown in fig. 5.1 whereas the refraction parameters are given in table 5.1.

Parameter	Value
γ_I	7/5
γ_{II}	5/3
\mathcal{M}_I	6.67 g/mol
\mathcal{M}_{II}	4 g/mol
P_0	1 bar
$T_{0,I}$	298 K
$T_{0,II}$	1138 K
(x, y)	(0.5cm, 3cm)
Initial i - m dist.	1cm

Table 5.1: Parameters for refraction at a $2H_2+1O_2$ - He interface.

Because the phase I gases are not noble but diatomic, the γ_I heat ratio may be different before and behind the shock. This could be tested by confronting perfect-gas shock wave theory, to results from Caltech's Shock and Detonation Toolbox [15]. The Shock and Detonation toolbox provides models that determine the post-shock state of a non-perfect gas [14].

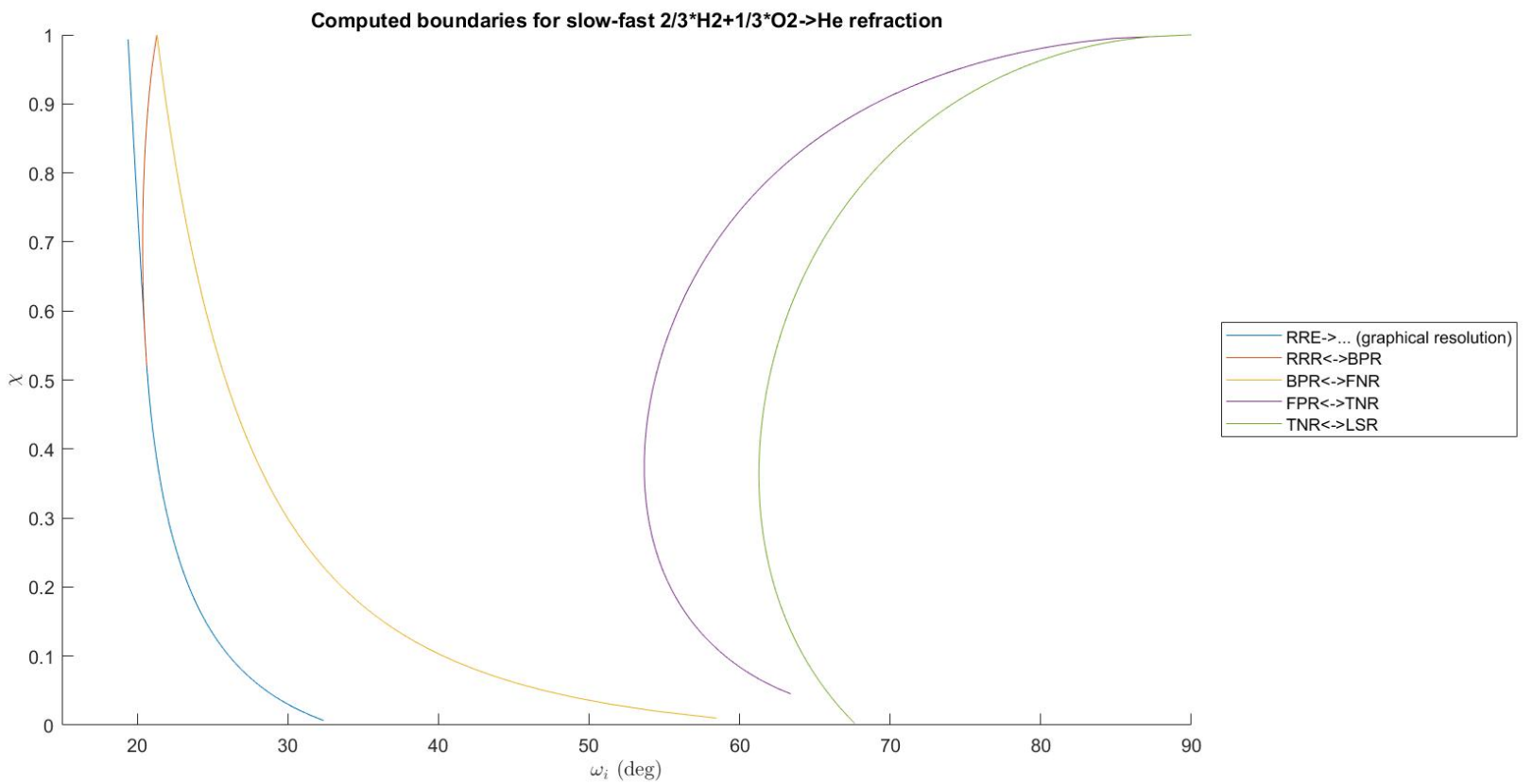


Figure 5.1: Theoretical refraction pattern boundaries for a $2\text{H}_2+1\text{O}_2\text{-He}$ slow-fast interface.

5.2 Lagrangian particles in RRE flows

In this section, we want the profiles of pressure, temperature, and specific volume for Lagrangian particles. Here, we will focus on the RRE pattern. The pressure and temperature fields before and after the wave are calculated as explained in section 3.3. The two following subsections detail how the profiles were calculated in each zone.

5.2.1 Initial conditions

The particle's initial conditions are detailed in fig. 5.2. Therefore when meeting the incident wave,

$$r_i = y - \frac{x}{\tan(\omega_i)}$$

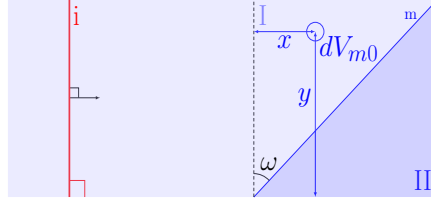


Figure 5.2: Initial particle position.

Where dV_{m0} is the Lagrangian particle at its initial state and r_i is defined in figure 5.2.

5.2.2 Flow pattern

In a RRE pattern, the particle is first compressed and heated when crossing the incident shock, then cooled down and expanded when crossing the expansion fan. Figure 5.3 shows the flow pattern considered to calculate the thermodynamic state along the path of a Lagrangian particle.

Geometrical parameters are defined in fig 5.3.

5.2.3 Before the expansion fan

Geometrical parameters: According to the Prandtl-Meyer expansion theory

$$\mu_1 = \arcsin\left(\frac{1}{M_r}\right)$$

This leads to

$$r_{e1} = r_i M_r \sin(\omega_i - \delta_1)$$

In addition

$$\theta_1 + \omega_i - \delta_1 + \mu_1 = \frac{\pi}{2}$$

Time spent in zone 1 is given by

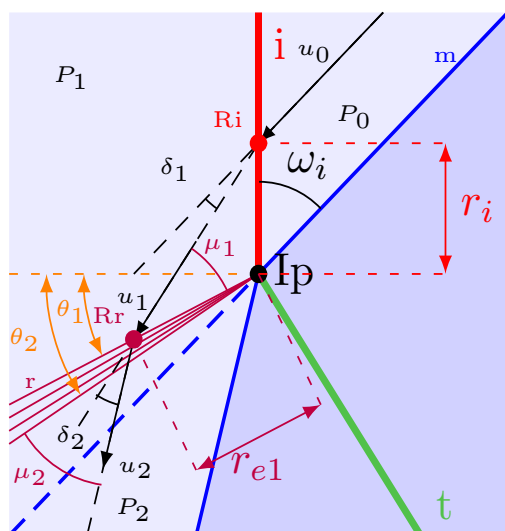
$$\Delta t_1 = \frac{r \cos(\theta_1)}{u_1 \sin(\mu_1)}$$

5.2.4 In the expansion fan

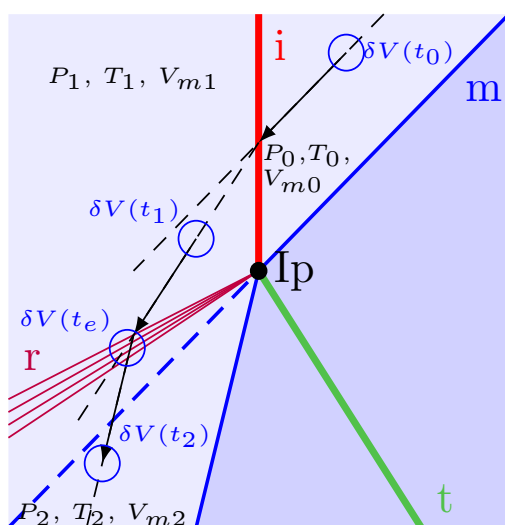
Infinitesimal discontinuities inside the expansion were considered to obtain the following equations. Another method using characteristics may have been more appropriate to follow Lagrangian particles.

Kinematic equations:

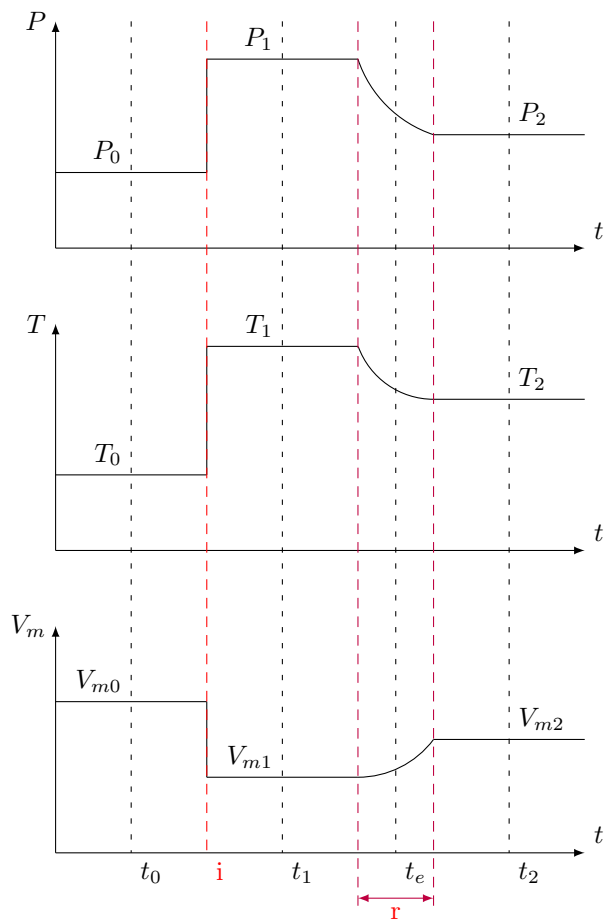
$$\begin{aligned} 0 &= d\theta + d\mu - d\delta & d\theta &= \frac{u_n}{r_e} dt \\ dr_e &= u_t dt, & u_t &= \text{const} \end{aligned}$$



(a) Angles in pattern



(b) Lagrangian particle path in Ip's frame of reference



(c) Pressure, temperature and specific volume profiles of a Lagrangian particle

Figure 5.3: Lagrangian particle in RRE pattern

Prandtl-Meyer expansion theory equations:

$$d\delta = \frac{\sqrt{M^2 - 1}}{2M^2 \sqrt{1 + \frac{\gamma_I - 1}{2} M^2}} d(M^2) \quad d\mu = -\frac{d(M^2)}{2\sqrt{M^4 - M^2}}$$

Isentropic flow equations:

$$\begin{aligned} du_n &= \frac{u_n}{2} \frac{d(M^2)}{1 + \frac{\gamma_I - 1}{2} M^2} & dV_m &= \frac{V_m}{2} \frac{d(M^2)}{1 + \frac{\gamma_I - 1}{2} M^2} \\ dP &= -\frac{\gamma_I P}{2} \frac{d(M^2)}{1 + \frac{\gamma_I - 1}{2} M^2} & dT &= T \frac{\gamma_I - 1}{2} \frac{d(M^2)}{1 + \frac{\gamma_I - 1}{2} M^2} \end{aligned}$$

5.2.5 Results

Calculated theoretical results for refraction at a $2H_2+1O_2$ - He interface are shown in figure 5.4. Using finite elements could be a way to validate results.

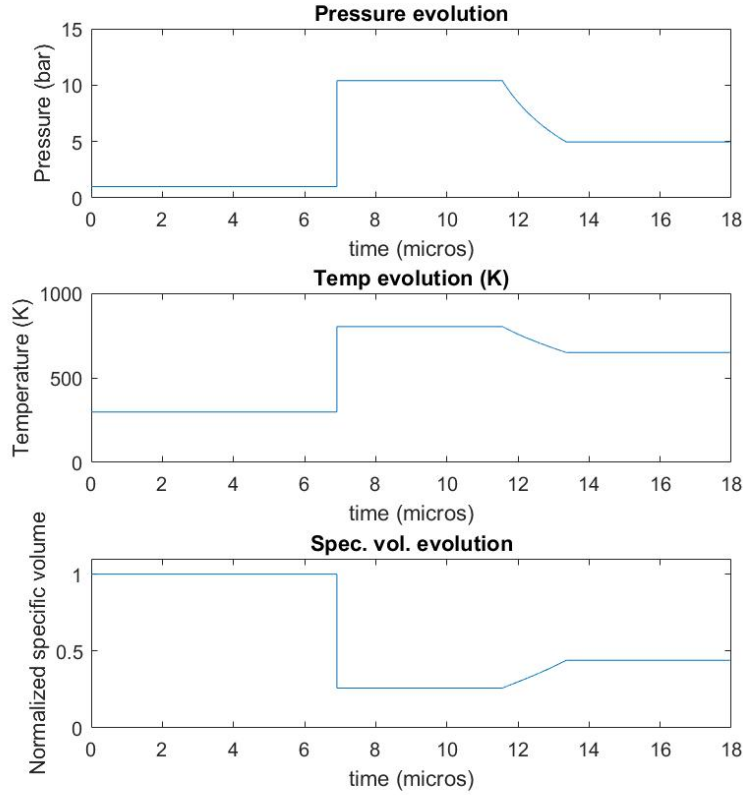


Figure 5.4: Evolution of thermodynamic variables along the path of a Lagrangian particle in a RRE pattern at a $2H_2+1O_2$ - He slow-fast interface.

5.3 Predicting mixture ignition

5.3.1 Insufficiency of chemical thermodynamics

The first approach was to use chemical thermodynamics to simulate the chemical process. This approach proved to be insufficient in predicting ignition.

The equilibrium constant was computed using Chemkin data fits of standard enthalpy [16, 3].

$$K^o(T) = \exp\left(-\frac{\Delta_r H^o(T)}{R_u T}\right)$$

where $\Delta_r H^o(T)$ is the standard enthalpy of reaction.

If $K^o(T) > 1$, the reaction is thermodynamically favored and if $K^o(T) < 1$, according to thermodynamics the reaction will not take place. It was however found that at lower temperatures, the reaction was more likely to take place than at high temperatures. This contradicts the idea that if a combustible mixture is heated, it is more likely to ignite.

This can be explained with Van't Hoff's law:

$$\frac{d \ln K^o}{dT} = \frac{\Delta_r H^o(T)}{R_u T^2}$$

and because for combustion, $\Delta_r H^o(T) < 0$, $K^o(T)$ decreases with T .

This approach was applied to the $H_2 + \frac{1}{2}O_2 \rightarrow H_2O$ reaction and figure shows a plot of $K^o(T)$ as a function of T .

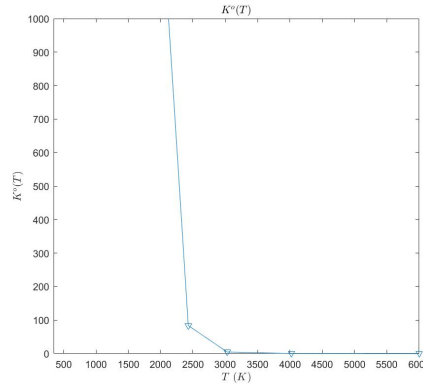
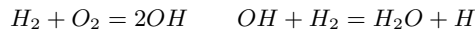


Figure 5.5: $K^o(T)$ for $H_2 + \frac{1}{2}O_2 \rightarrow H_2O$ reaction as a function of temperature.

5.3.2 Kinetic criterion

For future work, the chemical kinetic equations could be integrated along a Lagrangian particle path to evaluate where and when ignition would take place. A kinetic model of the combustion reaction is necessary to explain why combustion is more likely to take place. Chemists use programs such as Chemkin to simulate the reaction.

Chemkin uses combustion chemical models that describe the combustion as a multitude of elementary reactions. For example, the combustion of an H_2 - O_2 mixture can be decomposed with the help of the following reactions:



Thermodynamic data fits mentioned in the previous section are then used to compute the thermodynamic transformation of the mixture. Kinetics and a modified Arrhenius equation are used to calculate reaction rates as

$$v = k \prod_i c_i^{m_i} \quad k = AT^n \exp\left(-\frac{E_a}{R_u T}\right)$$

where v is the reaction speed, c_i are reactant concentrations, m_i is the reactant order, k is the rate constant, and E_a is called the reactant speed.

Because here $E_a > 0$ reaction speed increases with T , so according to kinetics, combustion is more likely to happen at higher temperature.

Chapter 6

Conclusion

The purpose of this project was to develop a theoretical model for an experiment carried out at Tsinghua University to investigate a phenomenon occurring in combustion engines. The experiment was an RCM experiment (see figs 1.4, 7.1) to investigate a combustion process called “super-knock” that can severely damage internal combustion engines (see fig 1.3(c)). Because in this experiment a shock wave travels through fresh unburned gas and then a hot flame, the project aimed to apply shock wave refraction theory that was previously elaborated in various papers [1, 2, 7, 8, 9, 10, 11, 20, 13]. A calendar of the assigned tasks can be found in the appendices’ figure 7.2.

During the internship, we were able to reproduce most of Abd-El-Fattah and Henderson’s method for plotting the domains of experimental parameters in which certain wave refraction patterns may form. We were unable to reproduce one boundary of the pattern transitions, between FPR and TNR.

This method of predicting pattern domains was then applied to a different gas-gas interface. The computed domains were then confronted to finite element simulations. The pattern transitions in finite element simulations corresponded to a certain degree to the theoretical simulations.

Some ground work was laid to develop some theory for reactive cases. The pattern domains were plotted for a reactive case. We established the theory for following Lagrangian particle in a specific pattern (RRE). After reaching a dead-end simulating the reactive process purely with chemical thermodynamics, a very brief introduction to Chemkin-based simulations was done.

Some new perspectives are still possible. For instance, using S. Zeng and K. Takayama’s detailed theory [20] to plot the unmatched boundary. The pattern domains can be plotted using the ω angle between i and m instead of ω_i as done by Abd-El-Fattah and Henderson [1]. Other finite element simulations could be made: simulations with non perfect gases, with a curved interface, reactive refraction simulations, redoing the RCM simulation with higher numerical simulation in hopes of seeing how refraction may play a role. This project also opens up perspectives of shock wave refraction experiments that could be done at the CCE laboratory.

The project therefore focused on the fluid details of experiments done to imitate a car engine. It has led to the investigation of some details of shock wave refraction theory. Although the present project may seem actually far away from the original RCM experiment, the detailed examination of the shock refraction theory may eventually lead to important contribution at a fundamental level. This, in the hopes of eventually returning to the RCM experiment and super-knock theory.

Bibliography

Article

- [1] A.M. Abd-El-Fattah and L.F. Henderson. “Shock Waves at a slow-fast gas interface”. In: *J. Fluid Mech.* 89 (1976), pp. 79–95. DOI: <https://doi.org/10.1017/S0022112078002475>.
- [2] A.M. Abd-El-Fattah, L.F. Henderson, and A. Lozzi. “Precursor shock waves at a slow-fast gas interface”. In: *J. Fluid Mech.* 76 (1976), pp. 157–176. DOI: <https://doi.org/10.1017/S0022112076003182>.
- [7] L.F. Henderson. “On expansion waves generated by the refraction of a plane shock at a gas interface”. In: *J. Fluid Mech.* 30 (1967), pp. 385–402. DOI: <https://doi.org/10.1017/S0022112067001491>.
- [8] L.F. Henderson. “On shock impedance”. In: *J. Fluid Mech.* 40 (1970), pp. 719–735. DOI: <https://doi.org/10.1017/S002211207000040X>.
- [9] L.F. Henderson. “On the refraction of shock waves”. In: *J. Fluid Mech.* 198 (1989), pp. 365–386. DOI: <https://doi.org/10.1017/S0022112089000170>.
- [10] L.F. Henderson. “The refraction of a plane shock wave at a gas interface”. In: *J. Fluid Mech.* 26 (1966), pp. 607–637. DOI: <https://doi.org/10.1017/S0022112066001435>.
- [11] L.F. Henderson, P. Colella, and E.G. Puckett. “On the refraction of shock waves at a slow-fast gas interface”. In: *J. Fluid Mech.* 224 (1991), pp. 1–27. DOI: <https://doi.org/10.1017/S0022112091001623>.
- [13] R.R. Nourgaliev et al. “Shock wave refraction patterns at interfaces”. In: *International Journal of Multiphase Flow* 31 (2005), pp. 969–995. DOI: [10.1016/j.ijmultiphaseflow.2005.04.001](https://doi.org/10.1016/j.ijmultiphaseflow.2005.04.001).
- [17] Y. Wang et al. “Shock wave and flame front induced detonation in a rapid compression machine”. In: *Shock Waves* 28 (2018), pp. 1109–1116. DOI: <https://doi.org/10.1007/s00193-018-0832-2>.
- [18] Z. Wang, H. Liu, and Rolf D. Reitz. “Progress in Energy and Combustion Science”. In: *Shock Waves* 61 (2017), pp. 78–112. DOI: <http://dx.doi.org/10.1016/j.pecs.2017.03.004>.
- [20] S. Zeng and K. Takayama. “On the refraction of shock wave over a slow-fast gas interface”. In: *Acta Astronautica* 38 (1996), pp. 829–838. DOI: [https://doi.org/10.1016/S0094-5765\(96\)00096-3](https://doi.org/10.1016/S0094-5765(96)00096-3).

Book

- [19] Han Z. and Yin X. *Shock Dynamics*. Springer Netherlands, 1993. Chap. 8.1. ISBN: 978-94-017-2995-6. URL: <https://www.springer.com/gp/book/9780792317463>.

Manual

- [14] *Numerical Solution Methods for Shock and Detonation Jump Conditions*. 2015.
- [16] *THERMODYNAMIC DATA Core Utility Manual*. CHEMKIN Collection. Version 3.7.1.

Online

- [3] A. Burcat and B. Ruscic. *Ideal Gas Thermochemical Database with updates from Active Thermochemical Tables*. URL: <http://garfield.chem.elte.hu/Burcat/burcat.html>.
- [5] European Commission. URL: https://ec.europa.eu/clima/policies/transport/vehicles/cars_en.
- [6] Y. de Gouvello. *sw_detonation git project*. URL: https://github.com/2gouvy/sw_detonation.
- [15] *Shock and Detonation Toolbox - 2018 Version*. URL: <http://shepherd.caltech.edu/EDL/PublicResources/sdt/>.

Report

- [4] *China Vehicle Environmental Management Annual Report*. Ministry of Ecology and Environment, 2018.

Image

- [12] NASA. *Engine Power Train*. URL: <https://www.grc.nasa.gov/WWW/K-12/airplane/powert.html>.

Chapter 7

Appendices

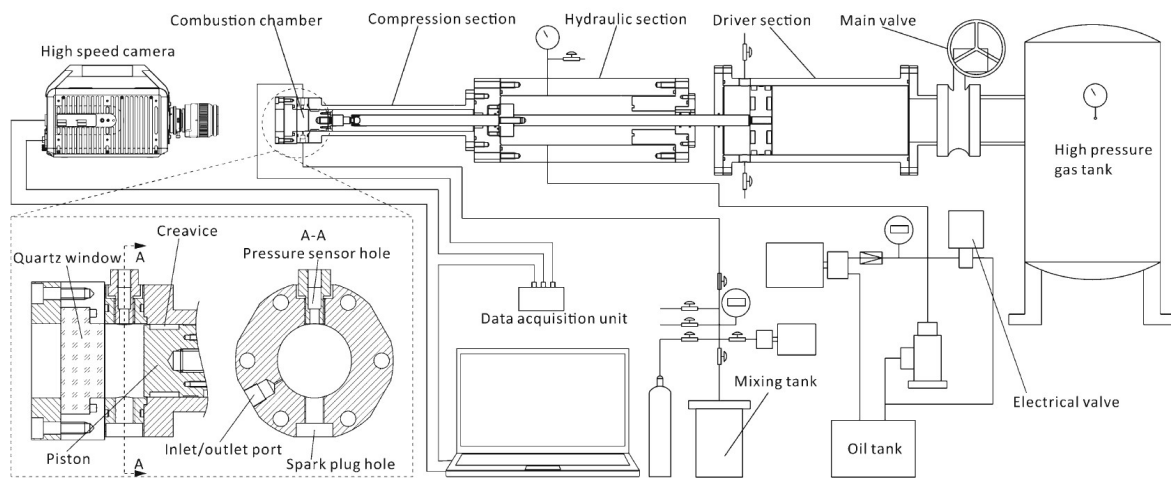


Figure 7.1: Schematic configuration of rapid compression machine (RCM) [17]

Week \ Task	03/06 - 09/06	10/06- 16/06	17/06- 23/06	24/06- 31/06	01/07- 07/07	08/07- 14/07	15/07- 21/07	22/07- 28/07	29/07- 09/08	05/08- 09/08	12/08- 09/08	19/08- 09/08
Reproducing pattern boundaries and polars from article												
Thermo- dynamic criteria												
Ar-He case and simulation discussion												
Lagran- gian particle												
Document -ing and tickz drawings												
Searching for explanation of theoretical boundary discrepancies (cf chapter IV)												

Figure 7.2: Weekly calendar of the assigned tasks (dates written in DD/MM format)